Causes of diverse impacts of ENSO on the Southeast Asian summer monsoon among CMIP6 models

Article

Accepted Version

www.reading.ac.uk/centaur

CentAUR

Central Archive at the University of Reading

Reading's research outputs online

Causes of Diverse Impacts of ENSO on the Southeast Asian Summer Monsoon Among CMIP6 Models

SHUHENG LIN,[a] BUWEN DONG,[b] SONG YANG,[a,c] SHAN HE,[d] AND YAMIN HU[e]

[a] *School of Atmospheric Sciences, Sun Yat-sen University; Southern Marine Science and Engineering Guangdong Laboratory (Zhuhai), Zhuhai, China*

[b] *National Centre for Atmospheric Science, Department of Meteorology, University of Reading, Reading, United Kingdom*

[c] *Guangdong Province Key Laboratory for Climate Change and Natural Disaster Studies, Sun Yat-sen University, Zhuhai, China*

[d] *School of Marine Sciences, Sun Yat-sen University; Southern Marine Science and Engineering Guangdong Laboratory (Zhuhai), Zhuhai, China*

[e] *Guangdong Climate Center, China Meteorological Administration, Guangzhou, China*

Revised for *The Journal of Climate*

August 2023

Corresponding author: Song Yang, yangsong3@mail.sysu.edu.cn

File generated with AMS Word template 2.0

1

ABSTRACT

This study examines the fidelity of 47 models from phase 6 of the Coupled Model Intercomparison Project (CMIP6) in representing the influence of El Niño–Southern Oscillation (ENSO) on the Southeast Asian summer monsoon (SEASM) during the ENSO decaying summer. The response of the SEASM to ENSO shows a large model spread among the models, some of which even simulate opposite signs of SEASM anomalies compared to the observed values. The bad-performance models (BPMs) are therefore selected to be compared with both the good-performance models (GPMs) and observations to explore the possible causes of the deficiency. Results show that in the BPMs, the ENSO-related warm sea surface temperature (SST) anomalies extend too far westward in the western equatorial Pacific (WEP) and they do not dissipate in the El Niño decaying summer in comparison with those in the GPMs and observations, interfering with the effect of ENSO on the SEASM. The slow decay of WEP SST anomalies from the El Niño mature winter to the decaying summer in BPMs is mainly caused by a weak negative shortwave radiation feedback due to a low sensitivity of convection to local SST anomalies, which is related to the cold bias in climatological SST over this region. On the other hand, from the mature winter to the decaying summer of El Niño, the El Niño-related anomalous eastward current does not reverse to westward current in the BPMs, which also contributes to the slow decay of WEP SST anomalies via inducing excessively persistent warm zonal advection.

SIGNIFICANCE STATEMENT

We investigate the possible causes of the diverse impact of El Niño–Southern Oscillation (ENSO) on the Southeast Asian summer monsoon (SEASM) among 47 CMIP6 models. We find that the plausible reason for the deficiency of some models in simulating the influence of ENSO on the monsoon is that the sea surface temperature (SST) anomalies associated with ENSO are unrealistic in the western equatorial Pacific (WEP) in these models. Further diagnoses indicate that the unrealistic WEP SST anomalies are related to the cold bias of the climatological SST, which could lead to a weak negative shortwave radiation feedback and excessively persistent warm zonal advection. The information provided in this study is useful for improving the skill of the climate models in representing the ENSO-SEASM relationship.

2

File generated with AMS Word template 2.0

1. Introduction

The Southeast Asian summer monsoon (SEASM), also called the western North Pacific (WNP) monsoon, is one of the important components of the Asian monsoon system. Differing from the two continental monsoon components, Indian summer monsoon and East Asian summer monsoon, the SEASM covers more oceanic regions with a core domain at about 120°E–160°E, 10°N–22°N of the WNP region (Wang and LinHo 2002; Li and Wang 2005; Chowdary et al. 2021). Its variations exert considerable impacts on the East Asian climate (Nitta 1987; Huang and Sun 1992; Lau et al. 2000; Wang et al. 2001; Li et al. 2016; Wang et al. 2016; Sun et al. 2022).

The interannual variability of the SEASM is strongly influenced by El Niño-Southern Oscillation (ENSO) and the mechanisms involved have been well documented. The ENSO exhibits a strong phase lock to the annual cycle, usually being mature in the boreal winter and decaying in the subsequent spring and summer (Tziperman et al. 1997; An and Wang 2001; Liao et al. 2021). However, the SEASM circulation and precipitation tend to be weaker (stronger) than normal during the El Niño (La Niña) decaying summer even if the warm (cold) sea surface temperature (SST) anomaly over the equatorial Pacific has disappeared (Huang and Wu 1989; Chang et al. 2000; Chou et al. 2009; Chen et al. 2012). This delayed impact of ENSO on SEASM is mainly built up through a WNP anomalous anticyclonic circulation (WNPAC), which forms in the El Niño mature winter and persists in the decaying spring and summer (Wang et al. 1999; Wang et al. 2000; Li et al. 2007). The El Niño-induced cold SST anomalies in the WNP during the El Niño mature winter can generate the WNPAC by stimulating a cold Rossby wave (Gill 1980), and then maintain the WNPAC during the following spring to summer via local air-sea interactions (Wang et al. 2000; Wu et al. 2017a,b). On the other hand, it is argued that the maintenance of the WNPAC also relies on remote forcing from the tropical Indian Ocean (TIO) warming during the El Niño decaying summer (Terao and Kubota 2005; Yang et al. 2007; Li et al. 2008; Xie et al. 2009; Wu et al. 2010). The TIO warming-induced anomalous heating can excite a warm Kelvin wave propagating eastward, causing suppressed convection and resultant anomalous anticyclone by inducing boundary-layer Ekman divergence over the WNP (Yang et al. 2007; Xie et al. 2009; Wu et al. 2010). The El Niño teleconnection causes warm SSTs in TIO like a battery charging capacitor, and then the TIO warming conveys the delayed influence of ENSO on the SEASM like a discharging capacitor, called as Indian Ocean capacitor effect (Xie et al.

3

2009). In addition to the TIO warming, the El Niño-induced warm SST anomalies over the tropical North Atlantic may also act to enhance the anomalous WNPAC by stimulating a warm Kelvin wave to its east (Lu and Dong 2005; Rong et al. 2010), similar to the discharging process over the TIO. On the other hand, when an El Niño rapidly decays and transitions to a La Niña developing phase, the cold SST anomalies emerging in the equatorial Pacific during the El Niño decaying summer can also reinforce the WNPAC by stimulating the Rossby wave in the northwest (Wang et al. 2013; Xiang et al. 2013). Furthermore, the cold SST anomalies would contrast with the TIO warming, resulting in an increased zonal gradient of SST anomalies, which could favor a stronger WNPAC as well (Terao and Kubota 2005; Chen et al. 2012; Cao et al. 2013; He and Zhou 2015; He et al. 2022). Thus, the important role of El Niño decaying pace in modulating the El Niño-WNPAC relationship has been recognized recently (Chen et al. 2016b; Jiang et al. 2019; Wu et al. 2020).

Given that the changes in the SEASM could exert tremendous socioeconomic impacts throughout East Asia, it is important to predict the variation of the monsoon. The accuracy of prediction is largely dependent on the ability of models in representing the ENSO-SEASM relationship (Lee et al. 2011). Recent studies have evaluated the performances of coupled general circulation models (CGCMs) participating in the Coupled Model Intercomparison Project Phase 3 (CMIP3; Meehl et al. 2007) and Phase 5 (CMIP5; Taylor et al. 2012) in simulating the relationship between ENSO and the SEASM (Song and Zhou 2014; Tao et al. 2016; Wu and Zhou 2016; Jiang et al. 2017; Feng et al. 2019). Song and Zhou (2014) found that the simulation skill for the interannual variability of the monsoon was improved from CMIP3 to CMIP5, although the CMIP5 models still simulated a weaker magnitude of the WNPAC during the El Niño decaying summer. They suggested that the improvement was due to a better reproduction of the TIO-WNPAC teleconnection. Tao et al. (2016) further suggested that the bias of models in representing the WNPAC might be caused by the unrealistic warm SST anomalies in the western equatorial Pacific (WEP) during the El Niño decaying summer, which led to a westward extension of the Rossby wave from the Pacific, weakening the effect of the Kelvin wave from the TIO warming. Jiang et al. (2017) also argued that the SST anomaly bias in the WEP was the main reason that some CMIP5 models could not simulate the El Niño–SEASM relationship correctly. By conducting a series of diagnostic analyses, they further suggested that the unrealistic SST anomalies over the WEP region during the ENSO decaying summer might be related to the excessive westward extension of cold tongue in these models, which could increase the climatological zonal SST

4

File generated with AMS Word template 2.0

gradient and thus cause a warmer zonal advection in the WEP. Besides, Feng et al. (2019) found that the climatological SST bias in some CMIP5 models could create strong warm meridional advection to cause a long-lasting central Pacific El Niño (Ashok et al. 2007; Kao and Yu 2009), which might be a reason for the failure of models to reproduce the WNPAC during the central Pacific El Niño decaying summer.

Recently, the outputs from the latest climate system models for CMIP6 have been released (Eyring et al. 2016). The CMIP6 models have been improved in comparison with the previous generations in many aspects, including the dynamic core and parameterizations for physical processes (Eyring et al. 2019; Jiang et al. 2020; Xin et al. 2020), but it is still unknown whether the impacts of ENSO on the SEASM have been improved in the CMIP6 models. Therefore, the main goal of this study is to address the following questions using the output from 47 CMIP6 model simulations. (1) How are the impacts of ENSO on the SEASM simulated in the CMIP6 models? (2) What is the model spread of these impacts? (3) What are physical processes responsible for the model spread of ENSO's influences on the SEASM?

The remainder of this paper is structured as follows. The datasets and analysis methods are introduced in Section 2. Section 3 evaluates the performance of CMIP6 models in simulating the relationship between ENSO and SEASM. In Section 4, the diverse impacts of ENSO on the SEASM are investigated and the primary source of different impacts is identified. The physical processes responsible for the primary source of diverse ENSO impacts are investigated in Section 5. Finally, conclusions and a further discussion are given in Section 6.

2. Data and methods

a. Datasets

The data analyzed in this study include 1) the monthly SST data from the Hadley Centre Sea Ice and Sea Surface Temperature (HadISST) version 1 (Rayner et al. 2003) on a 1°×1° resolution from 1870 to the present; 2) the precipitation data from the monthly Global Precipitation Climatology Project (GPCP) version 2.2, available since 1979 with a spatial resolution of 2.5°×2.5° (Adler et al. 2003); and 3) the monthly wind field from the European Centre for Medium-range Weather Forecast (ECMWF) version 5 reanalysis (ERA5; Hersbach et al. 2020), with a resolution of 1°×1°. The monthly wind data from the National

5

Centers for Environmental Prediction/National Center for Atmospheric Research (NCEP/NCAR; Kalnay et al. (1996)) are also analyzed.

The monthly mean outputs from the historical simulation of 47 CMIP6 CGCMs (see Table S1 in the supplemental material) are also used and only the first realization (r1i1p1f1) of each model is adopted. The monthly atmospheric variables analyzed include precipitation, wind, surface shortwave (SW) and longwave (LW) radiation, and surface latent heat flux (LHF) and sensible heat flux (SHF). The monthly oceanic variables used include SST, zonal wind stress, oceanic potential temperature, current velocity, and mixed-layer depth. The analysis period is 1979–2014, which is selected because the reanalysis data and observed precipitation data are more reliable during the satellite era (post-1979) and most of the CMIP6 historical simulations are available up to 2014. We have also repeated our analyses using a longer period for 1950–2014 and found that overall our results remain unchanged. All model datasets are horizontally interpolated onto the same 2.5°×2.5° grid using a bilinear interpolation method. Anomalies in observations and CMIP6 simulations are obtained by calculating the deviations from the climatological cycle after the linear trend is removed. To focus on the ENSO-monsoon relationship on interannual timescale, a 4–108-month bandpass filter is applied to each dataset using the six-order Butterworth filter designed by Parks and Burrus (1987).

b. Methods

The SST anomaly averaged over the Niño-3.4 region (170°W–120°W, 5°S–5°N) during December–February (DJF) is used to depict ENSO intensity and variability. The ENSO developing and decaying years are referred to as year (0) and year (1), respectively. Therefore, the ENSO mature winter is symbolized as D(0)JF(1), and the following spring (March–May) and summer (June–August) are indicated as MAM(1) and JJA(1), respectively. The SEASM index is defined as the horizontal shear of 850-hPa zonal winds between 90°–130°E, 5°–15°N and 110°–140°E, 22.5°–32.5°N (Wang and Fan 1999), which is used in studies of the East Asian–western Pacific and Southeast Asian summer monsoons (e.g., Yoo et al. 2006; Li and Yang 2017, Lu et al. 2021, 2023). A negative index value means an anomalous anticyclonic circulation in the region and represents a weak SEASM. In this study, the anomaly fields are regressed onto the DJF Niño-3.4 index to represent the ENSO-induced anomalies, as shown in the following equation:

File generated with AMS Word template 2.0

$$Y' = A * \text{Niño3.4} + \text{Res} \quad (1)$$

, where Y' is the anomaly of a variable, the regression coefficient A represents the ENSO-related anomalies without considering the influence of ENSO amplitude (per 1K Niño-3.4 index change induced anomalies), and Res is the residual. It has been argued that the ENSO-SEASM relationship also depends on ENSO amplitude in observations (Wang et al. 2008). The anomaly fields are also regressed onto the standardized Niño-3.4 index (Niño3.4_{std}) to assess the influence of ENSO amplitude by the following equation:

$$Y' = B * \text{Niño3.4}_{std} + \text{Res} \quad (2)$$

. Here, the regression coefficient B represents the response of SEASM to ENSO that contains both the influence of ENSO amplitude and non-amplitude factor A (Jiang et al. 2018), since $B \approx A * \sigma$ can be yielded by combining $\text{Niño3.4}_{std} = \frac{\text{Niño3.4}}{\sigma}$ and Eqs. (1) and (2) (Wu et al. 2021), where σ is the standard deviation of the DJF Niño-3.4 index (i.e., ENSO amplitude). A larger (smaller) ENSO amplitude thus leads to a stronger (weaker) monsoon. Therefore, the ENSO-induced SEASM anomalies are affected by both ENSO amplitude and the ENSO-monsoon relationship. The role of A is more complicated because even if the ENSO amplitude varies slightly among models, the atmospheric anomalies caused by ENSO could still show large diversity (Wu et al. 2021; He et al. 2022). Figure S1 in the online supplemental material verifies that the diversity in B is mainly determined by the diversity in the non-amplitude factor A rather than that in ENSO amplitude among the CMIP6 models. Thus, the non-amplitude factor A is the major focus of this study. In addition, the inter-model correlation between A and σ is 0.19, indicating that the diversity in A is also not determined by the diversity in ENSO amplitude (Fig. S1c).

It should be pointed out that the regression analysis does not discern the asymmetry between El Niño and La Niña, which is strong in observations (Fig. S2a). However, the ENSO asymmetry is significantly underestimated in both CMIP3 (Sun et al. 2013) and CMIP5 models (Zhang and Sun 2014), as well as in CMIP6 models (Zhang and Sun 2022). Figure S2 demonstrates that the ENSO asymmetries in terms of the center of SST anomaly, amplitude, and persistence are significantly underestimated in the CMIP6 models. As a result, there are weak asymmetries between the response of SEASM to El Niño and that to La Niña (Fig. S2f, i). The linear regression method used in this study, therefore, can reasonably represent the response of SEASM to ENSO in the CMIP6 models.

File generated with AMS Word template 2.0

To explore the dynamic and thermodynamic processes affecting the evolution of SST anomaly in the WEP during the ENSO decaying summer, a heat budget analysis of mixed-layer temperature anomalies is conducted. The equation governing the mixed-layer temperature can be expressed as:

$$\frac{\partial T'}{\partial t} = \underbrace{-u'\frac{\partial \bar{T}}{\partial x}}_{ZA} \underbrace{-v'\frac{\partial \bar{T}}{\partial y}}_{VA} \underbrace{-W_e'\left(\frac{\overline{T-T_e}}{h}\right)}_{EK} \underbrace{-\left(\bar{u}\frac{\partial T'}{\partial x} + \bar{v}\frac{\partial T'}{\partial y}\right)}_{MA} \underbrace{-\overline{W_e}\left(\frac{(T-T_e)'}{h}\right)}_{TH}$$

$$\underbrace{-\left(u'\frac{\partial T'}{\partial x} + v'\frac{\partial T'}{\partial y} + W_e'\frac{(T-T_e)'}{h}\right)}_{NDH} + \underbrace{\frac{Q'_{net}}{\rho_0 C_p h}}_{Q} + R \quad (3)$$

, where an overbar denotes monthly climatology and a prime denotes monthly anomaly. T means the potential temperature of sea water averaged in the mixed layer, which is a good proxy of SST. T_e is the potential temperature below the mixed layer. U and V denote the zonal and meridional horizontal current velocities averaged in the mixed layer, respectively. W_e represents the vertical entrainment velocity, calculated as $W_e = (\partial h/\partial t) + (\partial hu/\partial t) + (\partial hv/\partial t)$. Q_{net} is the net surface heat flux (positive downward), including net SW, LW, LHF and SHF. Note that we do not introduce the shortwave radiation penetrating through the ML (Q_d) here and put its effect in the residual term, because most historical simulations of the CMIP6 models do not output the variable that can measure it directly. Besides, Q_d is small in the western-central equatorial Pacific where the ML depth is usually larger than 40 meters (Wang and McPhaden 2001; Qu 2003). $\rho_0 C_p$ is the specific heat capacity per unit volume, where the seawater density ρ_0 is 1.029×10^3 kg m^{-3}, and the specific heat capacity C_p is 3996 J kg^{-1} K^{-1}. h is the mixed-layer depth, which is defined based on meeting a "sigma-t (density)" criterion introduced by Levitus (1982) in the CMIP6 models. The critical density difference for the criterion is typically about 0.03 kg m^{-3} (Griffies et al. 2016). On the right side of Eq. (3), the first and second terms denote the advection of mean temperature by anomalous zonal and meridional ocean currents, namely anomalous zonal advection term (ZA) and meridional advection term (VA), respectively. The third term involves the vertical advection induced by the Ekman pumping (EK). The next term represents the advection of anomalous temperature by the mean ocean current (MA), including the advection induced by mean zonal current (MAU) and mean meridional current (MAV). The vertical advection of heat from beneath the ML base associated with the mean entrainment velocity is usually referred to as the thermocline feedback term (TH). The nonlinear advection is usually

8

File generated with AMS Word template 2.0

referred to as nonlinear dynamical heating (NDH). R is the residual term, representing the sum of the unresolved physical processes such as turbulent mixing and diffusion, the accumulation of errors from the terms estimated directly (Hayes et al. 1991), and the neglected solar penetration.

In this study, the statistical significance of the regressed anomalies in observations is measured based on the two-tailed Student's t-test. To test the significance of the multimodel ensemble mean (MME) of the regressed anomalies, the confidence intervals are calculated by a bootstrapping method. We randomly select the regression anomaly of a single model with replacement from multiple models to obtain a subsample with the same number as the multiple models. Then a mean value of the subsample is calculated as a realization. This procedure is repeated 1000 times to construct 1,000 realizations. We then take the 2.5th and 97.5th percentiles of the realizations as the 95% confidence interval limits. The bootstrapping method is also used to test whether the difference in the MME of two groups of models is statistically significant. For each group of models, the mean value of a subsample is obtained based on the above procedure. Then the difference in the mean of two subsamples from two groups of models is calculated as a realization. We also repeat this 1000 times to construct 1,000 realizations of MME differences. The 95 % confidence interval thus can be obtained based on the statistical distribution of the 1,000 realizations.

3. Impacts of ENSO on the SEASM in CMIP6 CGCMs

Figure 1a shows the observed regression patterns of summer precipitation and 850-hPa winds against the Niño3.4 index of the previous winter. The most important feature is the significantly decreased rainfall over Southeast Asia, including the South China Sea, the Philippine Sea, and parts of the Indo-China Peninsula, with an anomalous anticyclonic circulation over the WNP. This result indicates that the SEASM tends to be weak (strong) than normal during the El Niño (La Niña) decaying summer, consistent with the previous findings (e.g. Chang et al. 2000; Chou et al. 2009; Chen et al. 2012). To evaluate the overall performance of CMIP6 models in simulating this ENSO-SEASM teleconnection, the MME of regressed anomalies of 47 CMIP6 CGCMs are also shown (Fig. 1b). Compared with observations, both the decreased rainfall and anomalous anticyclonic circulation are quite weak in the MME, and the main patterns show a significant eastward shift, which was also found in the MME of CMIP5 CGCMs (Tao et al. 2016; Jiang et al. 2017). Therefore, the

File generated with AMS Word template 2.0

MME of CMIP6 models does not show an apparent improvement in representing the response of the SEASM to ENSO in comparison with the CMIP5 models.
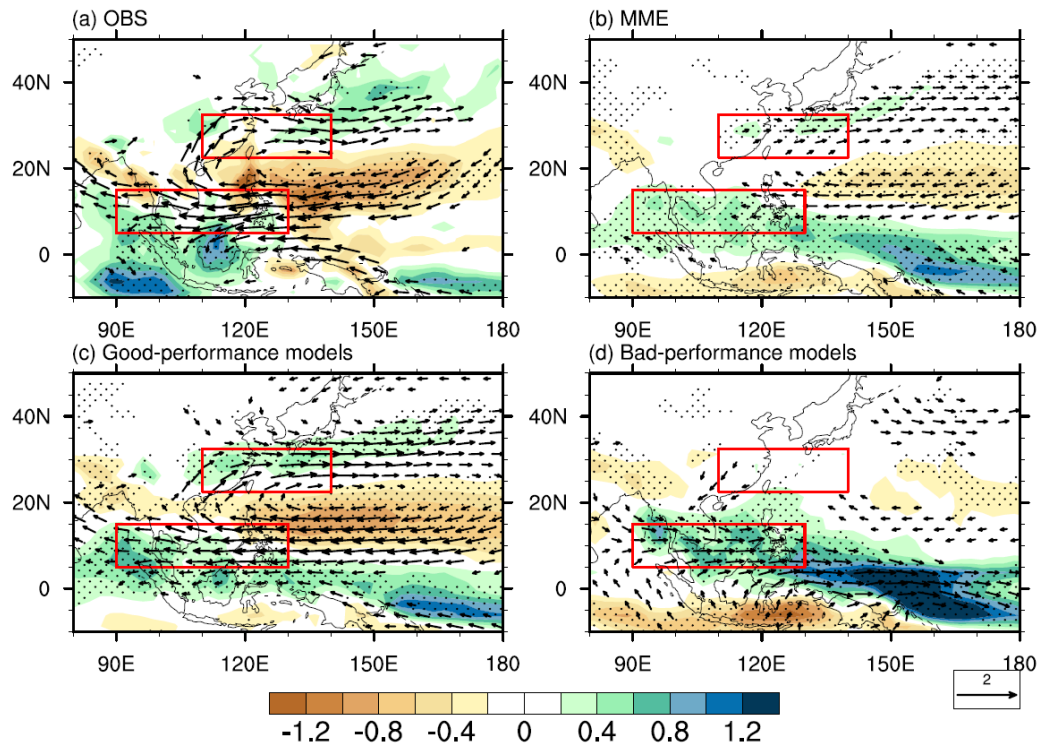
Fig. 1. Regressions of JJA(1) precipitation (shading; units: mm day^{-1}) and 850-hPa wind (vectors; units: m s^{-1}) anomalies onto the D(0)JF(1) Niño-3.4 index in (a) observations, (b) MME of 47 CMIP6 models, (c) GPMs, and (d) BPMs. The red boxes indicate the two domains (5°–15°N, 90°–130°E and 22.5°–32.5°N, 110°–140°E) used for defining the SEASM index. Black stippling indicates that the regressed anomalies are significant at the 95% confidence level. Only the wind vectors with significant values above the 95% confidence level are plotted.

We further examine the anomalous SEASM during the ENSO decaying summer in both observations and 47 models. There is a large diversity in the response of SEASM anomalies to ENSO among the CMIP6 models (Fig. 2). 14 out of the 47 models show much weaker values of negative SEASM index compared with observations (less than half of the observed values), and 13 models even simulate an enhanced SEASM during El Niño decaying summer. Nevertheless, some other models simulate comparable values, such as E3SM-1-1, EC-Earth3, E3SM-1-0, and ACCESS-CM2. Since most of the CMIP6 models show weaker values than observations, the MME simulates a quite weak SEASM index, consistent with the result shown in Fig. 1b. To better depict the diversity and identify the sources of the diverse impact of ENSO on SEASM, two groups of models are selected based on the 75th and 25th percentiles of SEASM index anomalies in the 47 CMIP6 models (Fig. 2). 12 models with the largest negative SEASM index anomalies above the 75th percentile are classified as good-performance models (GPMs), which simulate a SEASM index anomaly close to observations

10

File generated with AMS Word template 2.0

(red bars; Fig. 2). On the other hand, the 12 models with the largest positive SEASM index anomalies below the 25th percentile are classified as bad-performance models (BPMs) with the sign of SEASM index opposite to those of observations (blue bars; Fig. 2). As shown in Fig. 1c, the GPMs can reproduce the observed spatial patterns and the magnitudes of SEASM rainfall and circulation anomalies fairly well. By contrast, in the BPMs significantly increased rainfall, instead of decreased rainfall, can be found over the South China Sea and the Philippine Sea. Furthermore, westerly wind anomalies prevail over the off-equatorial eastern Indian Ocean and the western Pacific, with an anomalous cyclonic circulation over the South China Sea. Hence, the BPMs have quite low skill in simulating the observed impacts of ENSO on the SEASM. In general, by comparing the results in Fig. 1c and Fig. 1d with those in observations (Fig. 1a), it can be proved that the classification for good- and bad-performance models is reasonable. On the other hand, previous studies have suggested that the relationship between the ENSO and SEASM exhibits a decadal variation in both observations and climate models (Hu et al. 2014; Song et al. 2015). The BPMs may simulate a high ENSO-SEASM relationship in another period due to the decadal variation, and vice versa. The 36-yr running-regression of JJA(1) SEASM index onto D(0)JF(1) Niño-3.4 index indicates that the impacts of ENSO on SEASM indeed show prominent decadal variations in both GPMs and BPMs (Fig. S3 and Fig. S4). Nevertheless, in GPMs the running-regression coefficients are close to observations for most periods in the historical simulations (Fig. S3). However, in BPMs the regression coefficients deviate significantly from observations throughout the entire period in the historical simulations, and the BPMs could only simulate the significantly positive instead of the negative SEASM anomalies as in observations (Fig. S4), reconfirming that the classification is reasonable.

11

File generated with AMS Word template 2.0
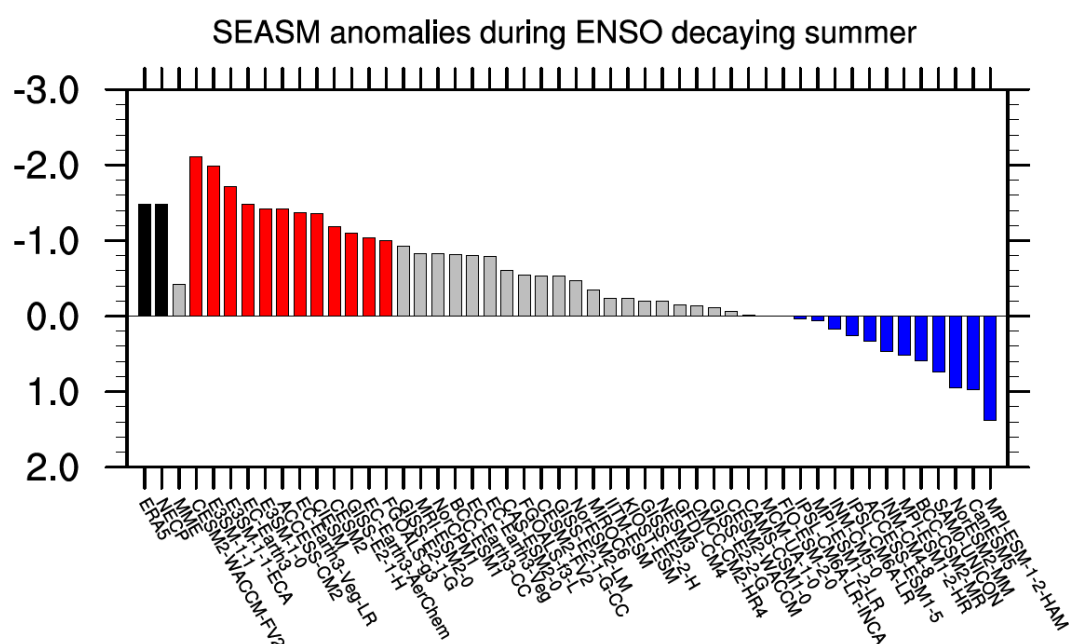
Fig. 2. Regressions of JJA(1) SEASM index (units: m s^{-1}) onto the D(0)JF(1) Niño-3.4 index in observations and 47 CMIP6 models. The black bars indicate the observed results based on ERA5 and NCEP-NACR datasets. The red (blue) bars highlight the twelve models with the largest (negative) SEASM index anomalies above (below) the 75th (25th) percentile of the SEASM anomalies in the 47 CMIP6 models.

4. Source of diverse impacts of ENSO on the SEASM

The primary source of the diverse impacts of ENSO on the SEASM among the CMIP6 models is discussed in this section by comparing the results among BPMs, GPMs, and observations. Figure 3 shows time evolutions of spatial patterns in the El Niño-related SST, 850-hPa wind, and precipitation anomalies in observations and the MMEs of GPMs and BPMs. During the El Niño mature winter, both GPMs and BPMs generally capture the main features of the observed SSTA pattern, with maximum SST warming in the central-eastern equatorial Pacific and SST cooling in both the south and the north of western Pacific (Figs. 3a, d, g). However, the warm SST anomalies extend westward too far into the west of WEP (west of 160°E) in the two groups of models, and the extension is slightly larger in the BPMs than in the GPMs, leading to a more westward shift of precipitation anomalies associated with El Niño (Figs. 3d, g). The excessive westward extension of ENSO-related SST anomalies has been well known in both CMIP3 and CMIP5 models (Collins et al. 2010; Kim and Yu 2012; Kug et al. 2012) and this bias still exists in most CMIP6 models as pointed out recently (Jiang et al. 2021). The cold SST anomalies in the WNP during the El Niño mature winter are comparable to observations (Fig. 3d), while they are underestimated in BPMs (Fig. 3g), corresponding to a weak WNPAC.

12

File generated with AMS Word template 2.0

From the El Niño decaying spring to summer, the observed SST anomalies in the equatorial central-eastern Pacific gradually decay and dissipate ultimately in summer, which are represented by both of GPMs and BPMs fairly well. Furthermore, the two groups of models also reasonably reproduce the observed SST warming in the TIO and NTA during the El Niño decaying summer. The evolutions of WEP SST anomalies in BPMs, however, display an apparent discrepancy from both observations and the GPMs. The SST anomalies in the WEP decay slowly from previous winter to the following spring and do not dissipate in the summer. Such bias in WEP SST anomalies is also found in the CMIP5 models that are not able to reproduce the observed ENSO-WNPAC teleconnection (Jiang et al. 2017; Jiang et al. 2018). By contrast, the WEP SST anomalies in GPMs are comparable to those in observations. In response to the prolonged SST warming in the WEP, there are positive precipitation anomalies and westerly wind anomalies over the WEP in BPMs, which is unfavorable for the maintenance of the anticyclonic circulation over WNP (Tao et al. 2016; Jiang et al. 2017). In addition, in BPMs the cold SST anomalies in the WNP do not persist after spring as in observations and GPM, which may also contribute to the formation of the bias in ENSO-WNPAC teleconnection.
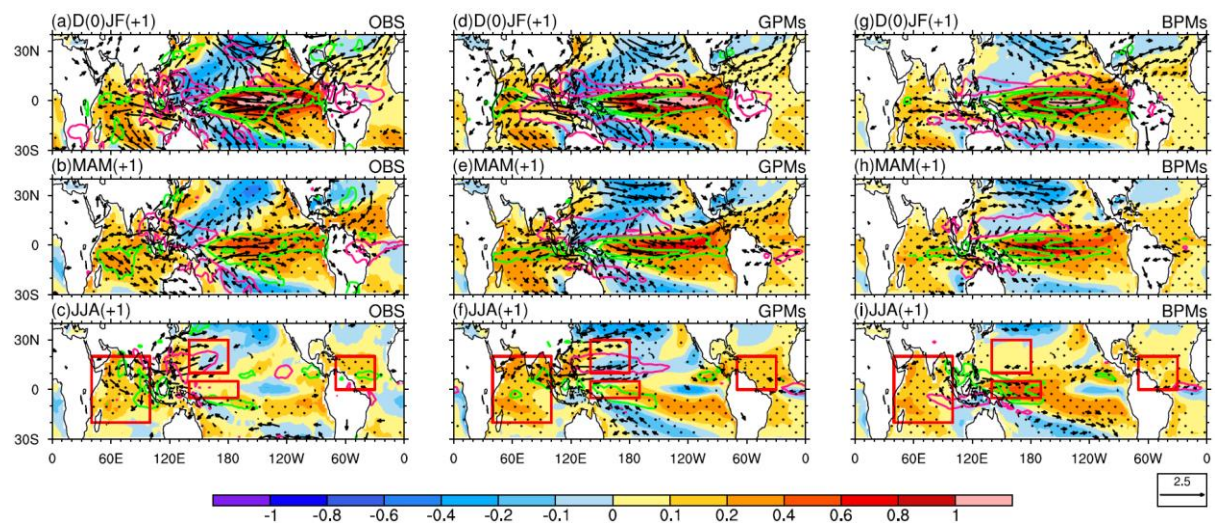
Fig. 3. Regressions of SST (shading; units: °C), precipitation (contours; units: mm day^{-1}) and 850-hPa wind (vectors; units: m s^{-1}) anomalies during (a) ENSO mature winter (D(0)JF(1)), (b) decaying spring (MAM(1)), and (c) decaying summer (JJA(1)) onto the D(0)JF(1) Niño-3.4 index in observations (wind field are derived from ERA5). (d)–(f) Same as (a)–(b), but for GPMs. (g)–(i) Same as (a)–(b), but for BPMs. Black stippling indicates that the regressed anomalies are significant at the 95% confidence level. Only the significant wind vectors above the 95% confidence level are plotted. The red boxes in (c)–(i) indicate the western equatorial Pacific (WEP; 5°N–5°N, 140°E–170°W), the western North Pacific (WNP; 10°N–30°N, 40°E–180°E), tropical Indian Ocean (20°S–20°N, 40°E–100°E), and tropical North Atlantic (0°–20°N, 70°W–30°W).

13

File generated with AMS Word template 2.0

To further illustrate the differences in the SST evolutions among the BPMs, GPMs and observations, the area-averaged of monthly regressed SST anomalies in the WEP, WNP, TIO, and NTA are shown in Fig. 4. Over the WEP, there is insignificant difference between GPMs and BPMs from the ENSO developing summer to mature winter (Fig. 4a), while the SST anomaly is significantly larger in models than that in observations due to the excessive westward extension of ENSO SST anomaly as we discussed above (Figs. 3d, g). Nonetheless, during the El Niño decaying summer, the magnitude of WEP SST anomaly in the GPMs is close to that in observations with a value below 0.1 °C, while it remains a value above 0.3 °C in the BPMs because of the significantly slower decline rate in BPMs from the subsequent spring to early summer (Fig. 4a). For the WNP, the observed cold SST anomaly starts to decay in May and dissipates in July, associated with a weakening positive air-sea interaction due to the changed direction of the mean flow (Fig. 4b). This result implies that the influence of WNP SST anomalies on the WNPAC weakens as summer progresses, consistent with the previous finding (Wu et al. 2010). The WNP SST anomalies in the GPMs have the same decay pace as in observations during summer, while the SST anomalies dissipate and turn into positive values in the BPMs (Fig. 4b). For both TIO and NTA, the SST warmings in the BPMs are comparable to those in both observations and the GPMs during the El Niño decaying summer (Figs. 4c, d). Moreover, the evolution of Niño3.4 SST anomalies in the BPMs is quite similar to that in both observations and the GPMs, indicating that there is no significant difference in ENSO decaying pace among the BPMs, GPMs and observations (Fig. S5). In general, the results in Fig. 4 suggest that the differences in SST anomalies between BPMs and GPMs during the ENSO decaying summer are most prominent in the WEP.

14
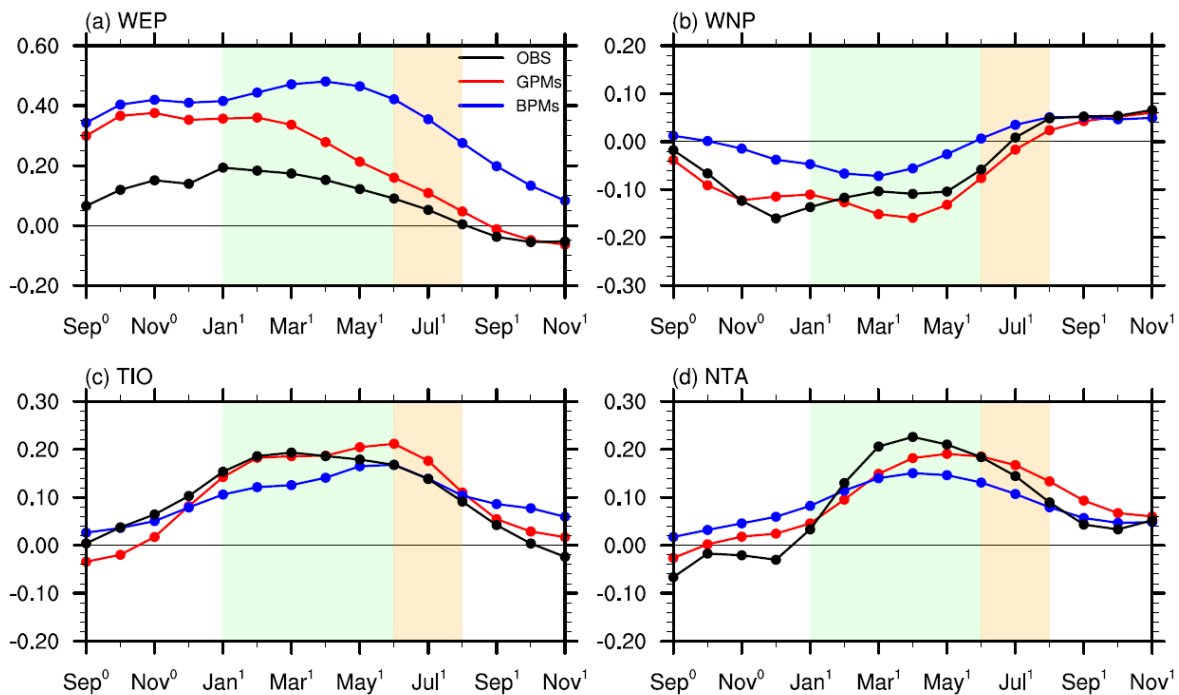
Fig. 4. (a) Time evolutions of monthly regressed SST anomaly (units: °C) in the western equatorial Pacific (WEP; 5°N–5°N, 140°E–170°W) upon the D(0)JF(1) Niño-3.4 index for the observation (black line), GPMs (red line), and BPMs (blue line). (b), (c), and (d) are the same as (a), but for the western North Pacific (WNP; 10°N–30°N, 140°E–180°E), tropical Indian Ocean (20°S–20°N, 40°E–100°E), and tropical North Atlantic (0°–20°N, 70°W–30°W), respectively.

To clarify the main source of the diversity of ENSO's impacts on the SEASM among CMIP6 models, Figs. 5a–d show the scatter plots between SEASM anomalies and the SST anomalies over the WEP, WNP, TIO, and NTA, respectively. The SEASM anomaly during ENSO decaying summer has a strongly positive inter-model correlation with the WEP SST anomaly, with a correlation coefficient of 0.63 exceeding the 99% confidence level. As a model simulates a larger warm SST anomaly in the WEP associated with El Niño, the model would represent a larger positive (i.e. smaller negative) SEASM anomaly (Fig. 5a). The correlation coefficients of SEASM anomaly with the WNP, TIO, and NTA SST anomaly are much lower than those with the WEP (Figs. 5b, c, d), indicating that the inter-model difference in simulated SEASM anomaly among the CMIP6 models is most sensitive to the WEP SST anomaly. Therefore, the large diversity in the ENSO-related SEASM anomalies is mainly caused by the large spread of the ENSO-related WEP SST anomalies among the CMIP6 CGCMs, which is the same as in CMIP5 models (Jiang et al. 2017).
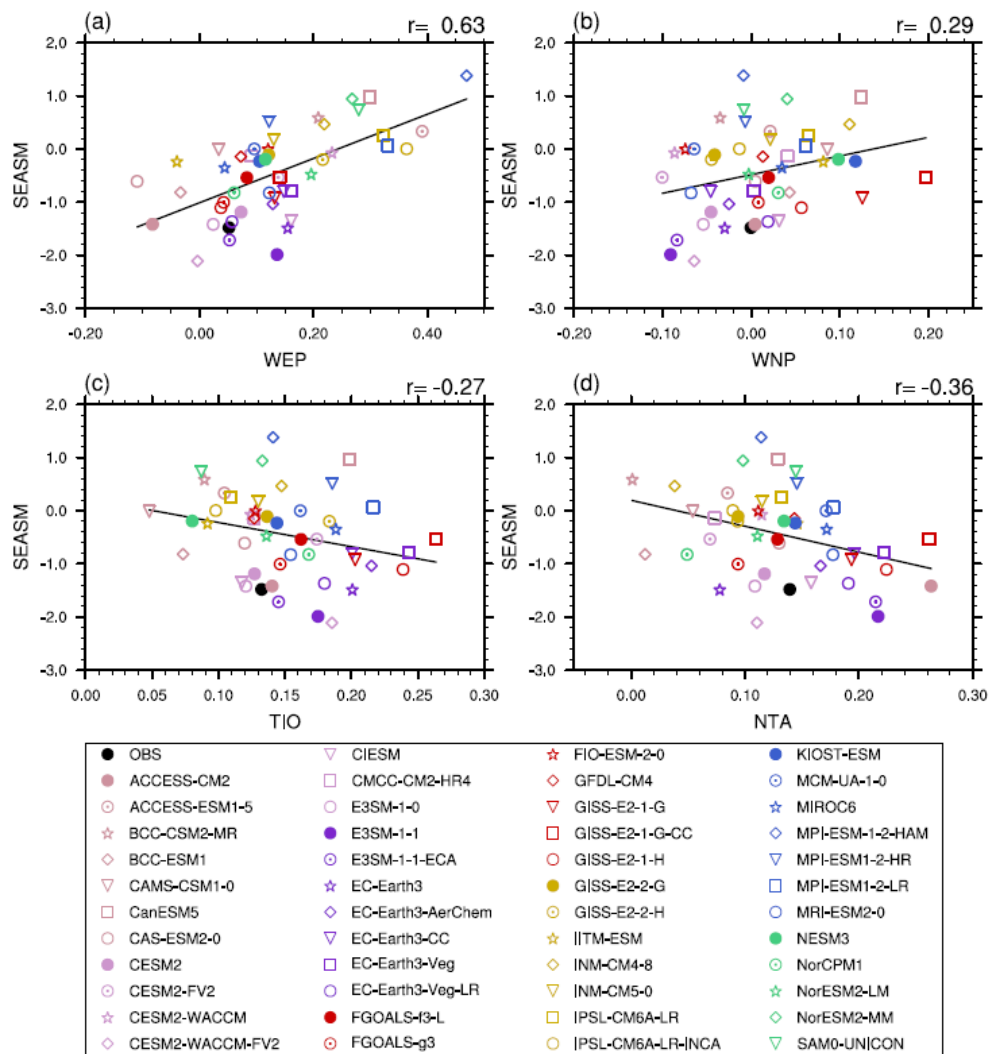
Fig. 5. Scatterplots of regressed JJA(1) SEASM anomalies vs the regressed JJA(1) SST anomalies of (a) WEP, (b) WNP, (c) TIO, and (d) NTA onto the D(0)JF(1) Niño-3.4 index in 47 CMIP6 models. Black dot denotes the observational result. Black lines denote the linear fit.

Based on a series of sensitivity experiments with an atmospheric general circulation model, Jiang et al. (2017) have demonstrated that the unrealistic warm SST anomalies over the WEP could induce anomalous cyclonic circulation and westerly wind anomalies in the WNP via exciting atmospheric stationary Rossby waves to its west, thereby interfering with the WNPAC in response to El Niño. In addition, the SST anomalies over the WEP could weaken the warm Kelvin wave emanating from the TIO by reducing the zonal gradient of SST anomalies between TIO and WEP (Terao and Kubota 2005; Cao et al. 2013; He and Zhou 2015; Jiang et al. 2017). To illustrate the influences of the bias of the WEP SST anomalies associated with ENSO in the CMIP6 models, the monthly evolutions of differences in regressed SST and 850-hPa wind anomalies between the BPMs and the GPMs are shown in Fig. 6. From January(1) to March(1), the differences in WEP SST anomalies

16

File generated with AMS Word template 2.0

between the two group of models are insignificant. The cyclonic circulation differences are associated with the positive SST differences over WNP due to the weaker cold SST anomalies over WNP in BPMs than those in GPM as we discussed above (Figs. 3d, g). Prominent differences in the WEP SST anomalies first appear in April(1) and grow gradually thereafter, accompanied with prominent westerly wind differences over the Indo-Pacific oceans. During July(1) and August(1), precipitation differences become significantly positive over WEP (Figs. 7g, h) when the warm SST differences is large (Figs. 6g, h). The prolonged WEP SST warming could induce positive rainfall anomalies *in situ*, thereby causing the anomalous cyclonic circulation over the WNP as atmospheric Rossby wave responses (Fig. 1d and Figs. S6e, f). Note that during June(1) a cyclonic circulation difference also exists over WNP (Fig. 6f) even though the difference in the WEP precipitation is insignificant (Fig. 7f). This is because the WNPAC and the associated deceased rainfall are well established in GPMs but weak in BPMs (Figs. S6a, d), which could be attributed to the weak SST gradient between TIO and WEP due to the bias of SST anomalies in WEP (Fig. 6f). For the GPMs, the atmospheric Kelvin wave forced by TIO warming are prominent, with low sea level pressure (SLP) on the equator of the Indian Ocean and surface northeasterly wind anomalies over the western Pacific (Fig. S7a), leading to the WNPAC via the Ekman divergence induced suppressed convection (Xie et al. 2009). However, the Kelvin wave-induced Ekman divergence mechanism does not work in the BPMs. The SLP anomalies in the WEP are lower than those in the Indian Ocean due to the prolonged SST warming (Fig. S7b). The surface northeasterly wind anomalies associated with the Kelvin wave, therefore, are offset by the westerly wind anomalies resulting from the SST gradient (Lindzen and Nigam 1987). Hence, in BPMs the WNPAC could not be reinforced by the TIO warming as in GPMs when the WNP cold SST anomalies become weaker during June(1). Overall, warmer SST anomalies over the WEP in the BPMs in comparison with those in the GPMs or observations could obstruct the formation and maintenance of the anomalous anticyclonic circulation during the El Niño decaying summer and cause above-normal SEASM precipitation. Also note that the precipitation differences and the SST differences are not collocated well over the WEP from January(1) to June(1) (Figs. 6a–f and Figs. 7a–f). This result will be discussed in the following section.

17

File generated with AMS Word template 2.0
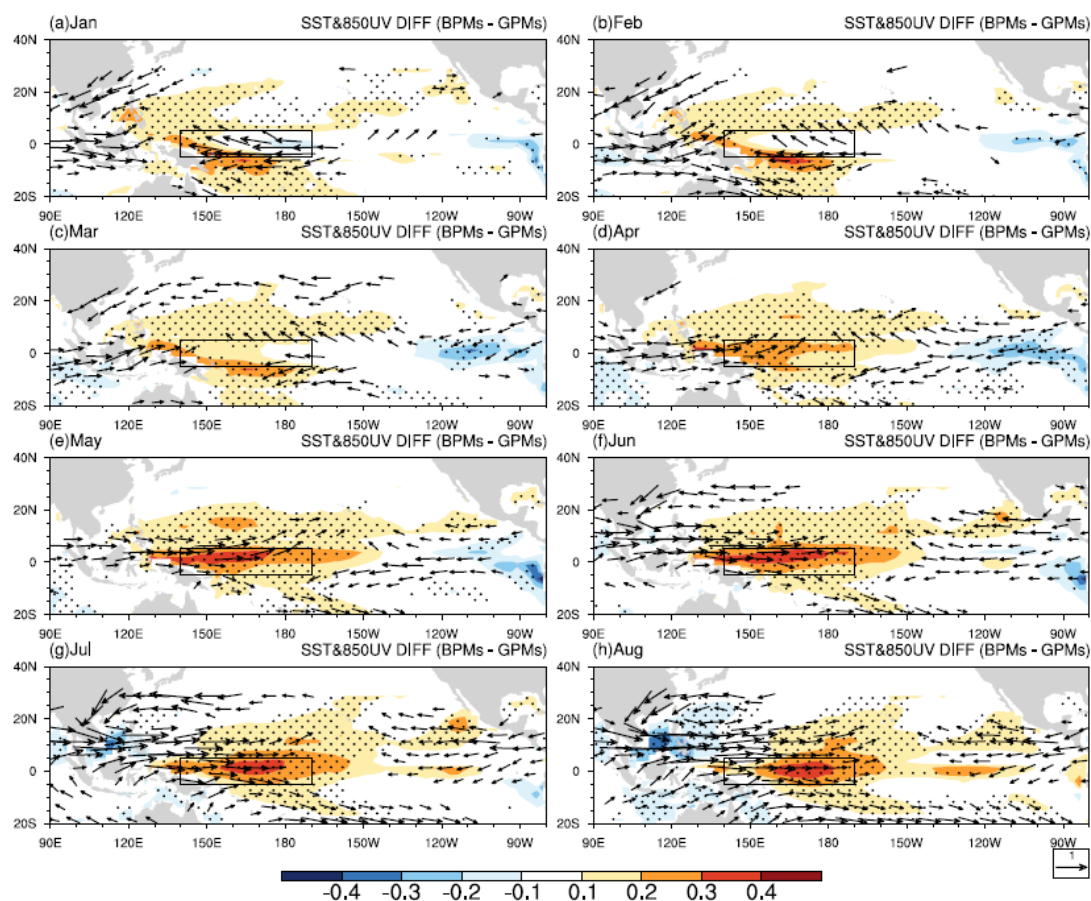
Fig. 6. Difference in the regressed SST (shading; units: °C) and 850-hPa wind anomalies (units: mm day^{-1}) onto the D(0)JF(1) Niño-3.4 index between GPMs and BPMs from January(1) to August(1) during ENSO decaying year. Black stippling indicates the 95% confidence level. Only the significant wind vectors above the 95% confidence level are plotted.

File generated with AMS Word template 2.0
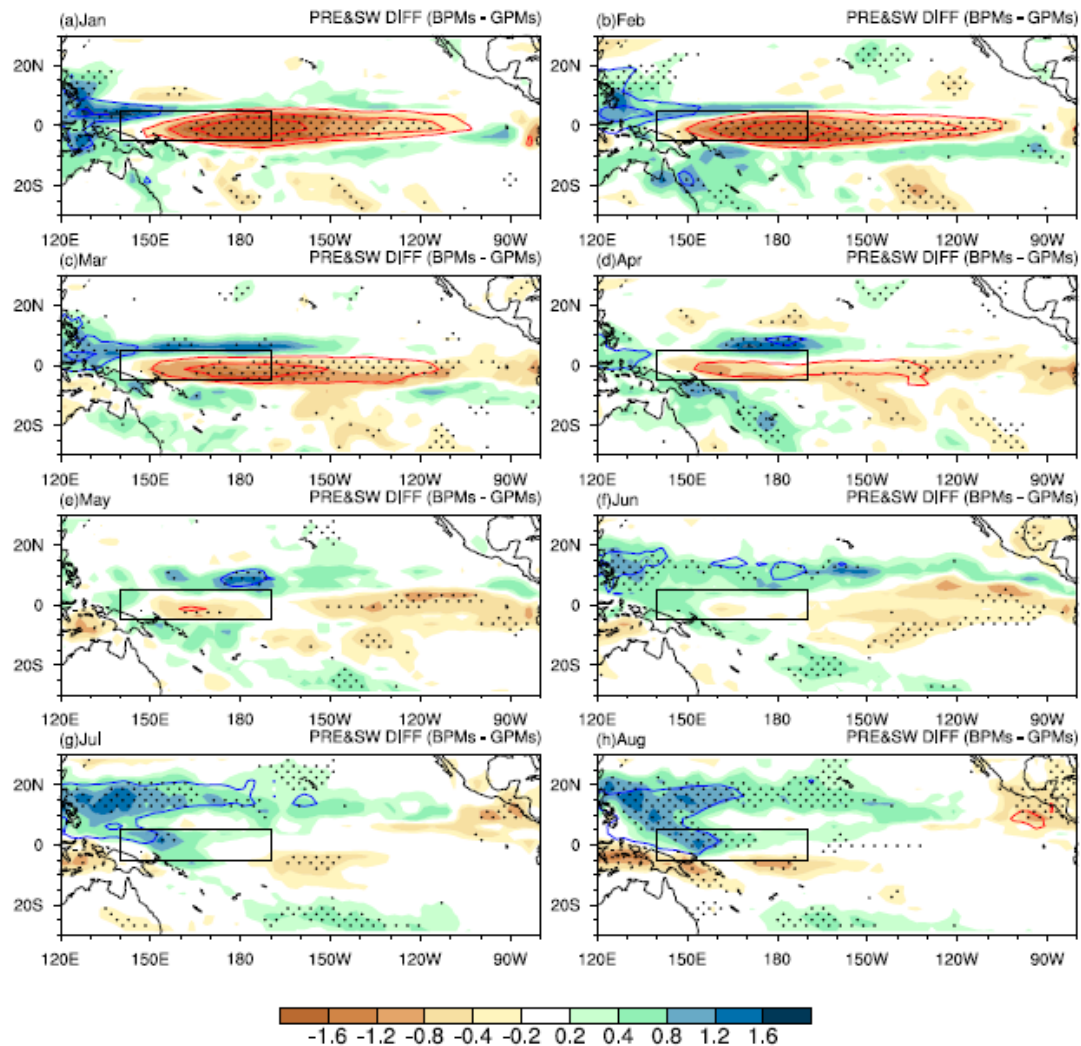
Fig. 7. Differences in regressions of precipitation (shading; units: mm day^{-1}) and shortwave radiation anomalies (contour; units: W m^{-2}) onto the D(0)JF(1) Niño-3.4 index between BPMs and GPMs from January(1) to August(1). Black stippling indicates the 95% confidence level. The black boxes indicate the western equatorial Pacific (5°S–5°N, 140°E–170°W).

5. Physical processes responsible for the unrealistic WEP SST anomalies in BPMs during ENSO decaying spring and summer

a. Mixed-layer heat budget

Given the fact that the bias in the WEP SST anomalies associated with ENSO exerts a significant impact on the SEASM, the cause of this bias needs to be further explored. Since the WEP SST anomalies decay more slowly in the BPMs than those in the GPMs and observations after ENSO peaks, the SST anomalies are significantly higher during the following summer in the BPMs (Fig. 4a). Therefore, we conduct a heat budget analysis of the oceanic mixed-layer temperature anomalies (MLTA) to elucidate physical processes

19

File generated with AMS Word template 2.0

responsible for the differences in the decay pace of the SST anomalies between the two groups of models. For the GPMs, the MLTA in the WEP decreases by about 0.25 °C from January(1) to July(1) (DT; Fig. 8). By contrast, the decrease in MLTA for the BPMs is quite small, consistent with the slower decay of the WEP SST anomalies (Fig. 4a). A further examination of the separate decomposition terms (Eq. 3) indicates that the difference in MLTA change is primarily contributed by the difference in the accumulated net heat flux (Q) anomaly between GPMs and BPMs, which is significantly smaller in the BPMs than that in the GPMs. On the other hand, the accumulated zonal advection term (ZA) also accounts for the small decrease in WEP SST anomalies in the BPMs, which is positive in the BPMs but negative in the GPMs. Note that there is also a pronounced difference in the advection process associated with the mean zonal current (MAU). However, this difference acts to reduce the difference in MLTA change between the two groups of models.
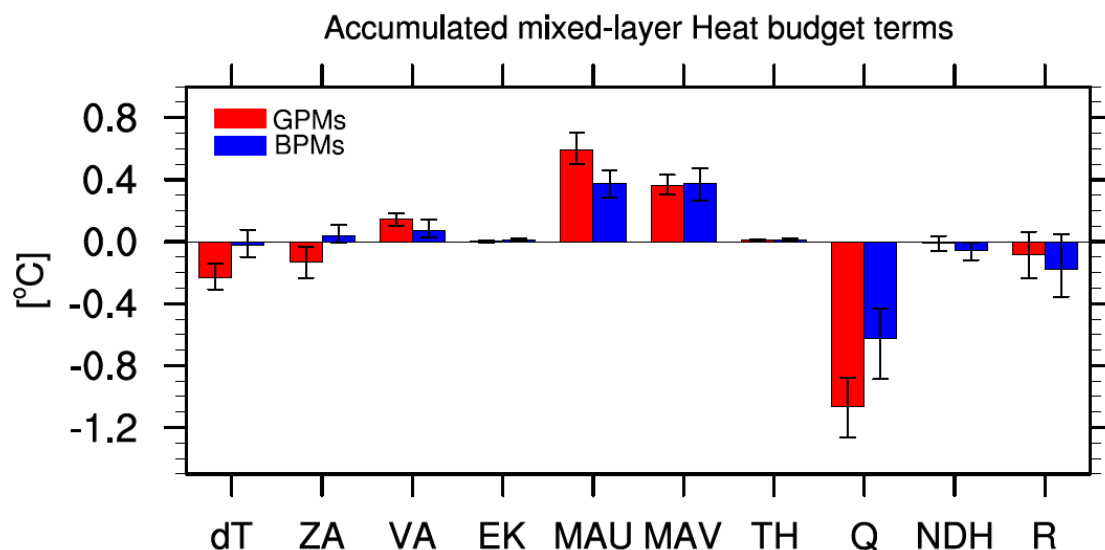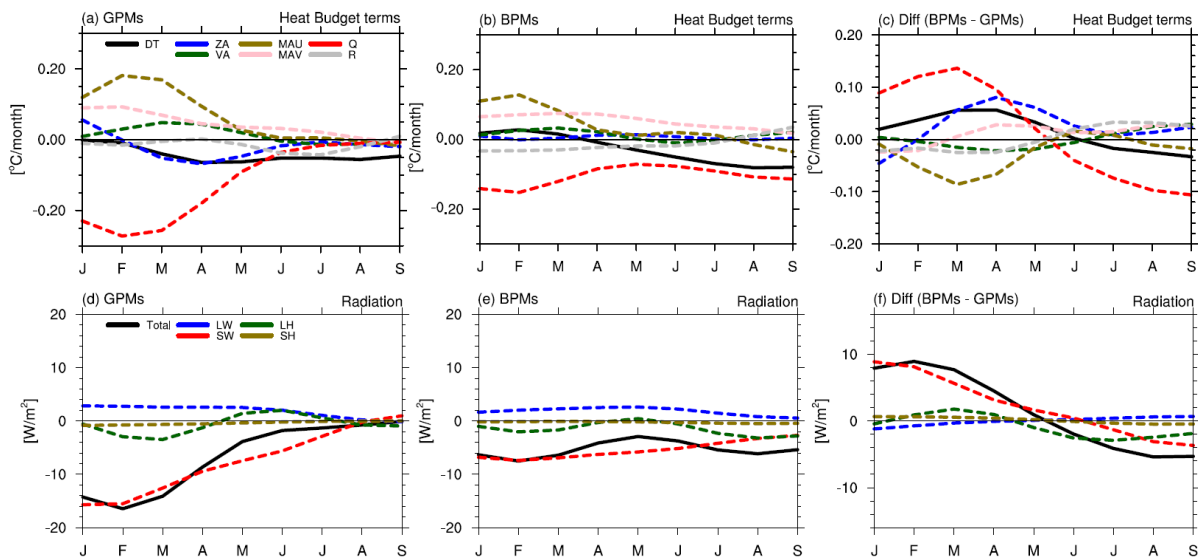

Fig. 8. Regressions of time-accumulated mixed-layer heat budget terms from January(1) to June(1) averaged within the western equatorial Pacific (5°S–5°N, 140E°–170°W) onto the D(0)JF(1) Niño-3.4 index. Red and blue bars denote the results of GPMs and BPMs, respectively. The error bars represent the 95% confidence intervals.

To further illustrate the relative contributions of these processes, the time series of heat budget terms are shown in Figs. 9a–c. Since the EK, TH, and NDH terms are quite small (Fig. 8), they are not discussed here. Compared with the GPMs, the negative tendency of MLTA is much smaller in the BPMs during El Niño mature winter and decaying spring, which is mainly caused by the smaller negative net heat flux during this period. On the other hand, the ZA term turns into a negative value after February(1) in the GPMs, but it is still positive throughout the El Niño decaying spring in the BPMs. The difference in the ZA term thus also contributes to the difference in MTLA tendency but plays a secondary role

20

File generated with AMS Word template 2.0

compared with the net heat flux. Since May, the differences in net heat flux become smaller than those in the ZA term, suggesting that the ZA term becomes more important in maintaining the slower decay pace of SST anomalies in the BPMs (Fig. 9c). A further decomposition of the net heat flux terms indicates that the differences in SW radiation dominate over the differences in net heat flux (Fig. 9f). The local SST warming in the WEP can induce deep convection and result in increased cloud cover (Figs. 3d, e), leading to reduced incoming SW radiation. The decreased downward SW radiation tends to cool the SST anomalies (Figs. 9d, e). This negative SW radiation feedback, however, is weaker in the BPMs compared with the GPMs and the physical processes responsible for these contrasting SW radiation feedbacks on SST anomalies are discussed in the next subsection.

Fig. 9. Time evolutions of regressed mixed-layer heat budget terms averaged within the western equatorial Pacific (5°S–5°N, 140E°–170°W) onto the D(0)JF(1) Niño-3.4 index from January(1) to September(1) during ENSO decaying year for (a) GPMs, (b) BPMs, and (c) their difference. (d), (e), (f) are the same as (a), (b), (c) but for total net heat flux and the associated radiation and turbulent fluxes on the ocean surface. Radiation and heat flux components are positive downward.

b. Negative shortwave radiation feedback

As shown in Fig.7, the differences in precipitation anomalies are prominent over the western-central equatorial Pacific during the January–March of El Niño decaying year, corresponding to the significant differences in the SW radiation incoming into the ocean surface (Figs. 7 a, b, c). As a boundary condition of the tropical atmosphere, warmer SST can provide conditions favorable for deep convection through enhancing moist static energy at the lower atmosphere (Zhang 1993) and by inducing the low-level convergence (Lindzen and Nigam 1987). However, the differences in WEP SST warming between the BPMs and the

21

File generated with AMS Word template 2.0

GPMs are insignificant from January to March (Figs. 6a, b, c). Furthermore, even when the WEP SST anomalies are significantly warmer in the BPMs than in the GPMs in April(1) and May(1) (Figs. 6d–f), there are no apparent differences in the precipitation over the WEP (Figs. 7d–f). These results imply that the response of deep convection to local SST anomalies over the WEP is weaker in the BPMs than in the GPMs, thereby causing the mismatch between the precipitation and SST differences.

To depict the sensitivity of convection response to local SST anomalies, the pointwise regression of precipitation anomalies onto SST anomalies is computed (e.g., He et al. 2018). In observations, an increase in SST corresponds to increased precipitation, indicating that *in-situ* SST warming favors an enhancement of deep convection (Fig. 10a). Besides, the regressed precipitation anomalies are larger in the western Pacific than in the central-eastern Pacific, because the sensitivity of convection change to SST anomalies depends on the local background SST. Convection is difficult to be generated when the local SST is lower than the so-called SST threshold around 27 °C (Gadgil et al. 1984; Graham and Barnett 1987; Johnson and Xie 2010). However, around the SST threshold, the intensity of deep convection increases dramatically with increasing SST. Even a small change in SST can greatly alter convection, indicating a high sensitivity of convection to SST (Waliser and Graham 1993; Zhang 1993; Lau et al. 1997). Furthermore, the sensitivity of convection to SST anomalies would increase with the increase in local background SSTs (He et al. 2018; Lin et al. 2022). The climatological SST in the western Pacific is higher than that in the central-eastern Pacific due to the existence of the Indo-Pacific warm pool and the equatorial Pacific cold tongue. Hence, a larger response of precipitation to SST anomalies exists in the WEP than in the central-eastern Pacific (Fig. 10a). This observed east-west contrast of precipitation sensitivity to local SST anomalies is reproduced in both GPMs and BPMs (Figs. 10b, c). However, significant discrepancies still can be found between these two groups of models. The GPMs perform well in simulating the observed intensity of precipitation sensitivity to SST over the WEP. By contrast, the sensitivity is significantly lower in the BPMs compared with the GPMs and observations (Fig. 10c). The WEP SST warming in the BPMs, therefore, could only induce a weak increase in precipitation, even though the magnitude of SST anomalies is close to that in the GPMs from January(1) to March(1) (Figs. 6a, b, c).

22

File generated with AMS Word template 2.0
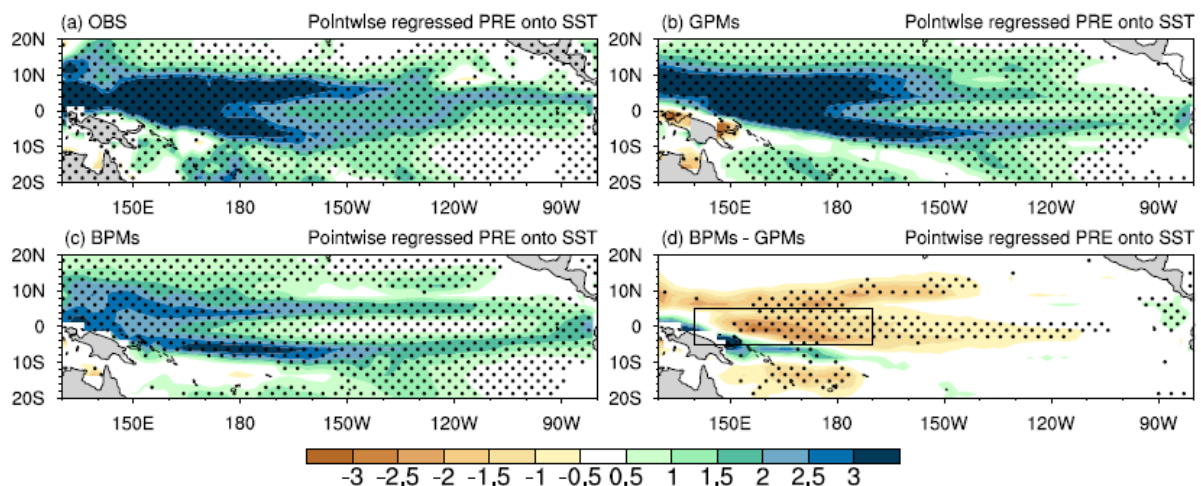
Fig. 10. Pointwise regressions of January–June averaged precipitation anomaly (shading; units: mm day⁻¹) onto SST anomaly for (a) observations, (b) GPMs, (c) BPMs, and (d) differences between BPMs and GPMs. Black stippling indicates the 95% confidence level. The black box in (d) indicates the western equatorial Pacific (5°S–5°N, 140°E–170°W).

The climatological SST distributions in observations, GPMs, and BPMs are shown in Fig. 11. For the GPMs, the spatial pattern and magnitude of SST climatology over the WEP are comparable to those in observations, although both the Pacific cold tongue and the boundary of warm pool in the equator show a slightly westward shift compared with the observed (Figs. 11a, b). But in the BPMs, the spatial extent of the warm pool shrinks more westward and the cold tongue extends excessively westward (Fig. 11 c). The WEP climatological SSTs in the BPMs are thus significantly lower than those in the GPMs (Fig. 11d), corresponding to the weaker sensitivity of precipitation to local SST anomalies in this region (Fig. 10d). One possible scenario that should be discussed is that, if the SST threshold is lower in the BPMs than in the GPMs and observations, the magnitude of WEP climatological SST relative to the SST threshold in the BPMs may be close to that in both GPMs and observations. As a result, the lower climatological SST over the WEP in the BPMs could also lead to a comparable sensitivity of convection to local SST anomaly with that in the GPMs and observations. It has been suggested that the tropical mean SST could be regarded as a proxy of SST threshold (e.g., Vecchi and Soden 2007; Johnson and Xie 2010). We thus check the relative SST over the Pacific in the two groups of models, which is obtained by the climatological SST subtracting the tropical mean SST (20°S–20°N). The WEP SSTs relative to the tropical mean SST in the BPMs are still lower than those in both observations and the GPMs (Fig. S8), and the tropical mean SST in the BPMs (27.26 °C) is very close to that in the GPMs (27.20°C), proving again that the low sensitivity of precipitation over the WEP to local SST anomalies could be attributed to the low climatological SST in the region.

23

File generated with AMS Word template 2.0

Note that the negative differences in precipitation anomalies associated with El Niño between BPMs and GPMs disappear and even turn into positive values from May(1) to June(1) (Figs. 7d, e), indicating that the influence of SW radiation differences is weakened. This is probably because the WEP SST anomalies in the BPMs have become significantly larger than those in the GPMs. The warmer WEP SST anomalies can offset the effect of the weaker precipitation sensitivity to local SST changes, resulting in comparable precipitation changes in the BPMs compared with the GPMs. After June(1), there is more increased precipitation and less incoming SW radiation over the WEP in BPMs than in GPMs since the warm SST anomalies still linger in the BPMs but have dissipated in the GPMs, corresponding to the turning point of the sign in the SW difference (Fig. 8f).
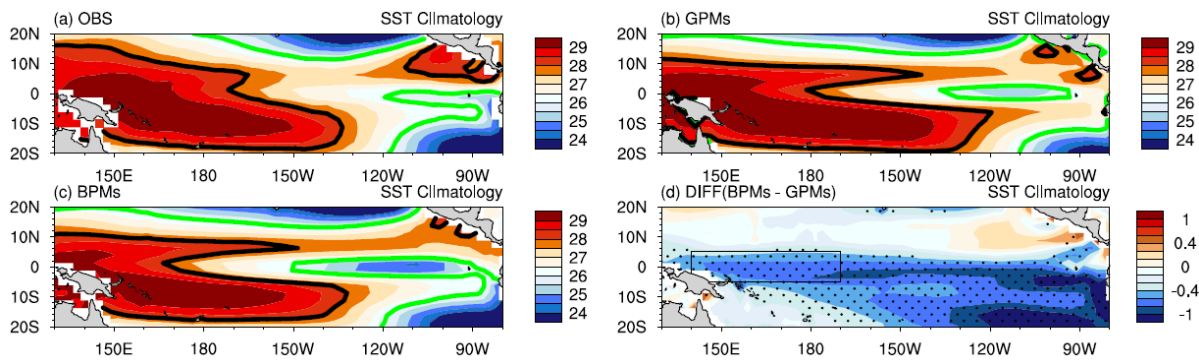
Fig. 11. Climatology of SST (shading; units: °C) during January–June for (a) observations, (b) GPMs, (c) BPMs, and (d) difference between BPMs and GPMs. The black and green contours denote the 28 °C and 26 °C isotherm lines, respectively. Black stippling indicates the 95% confidence level. The black box in (d) indicates the western equatorial Pacific (5°S–5°N, 140°E–170°W).
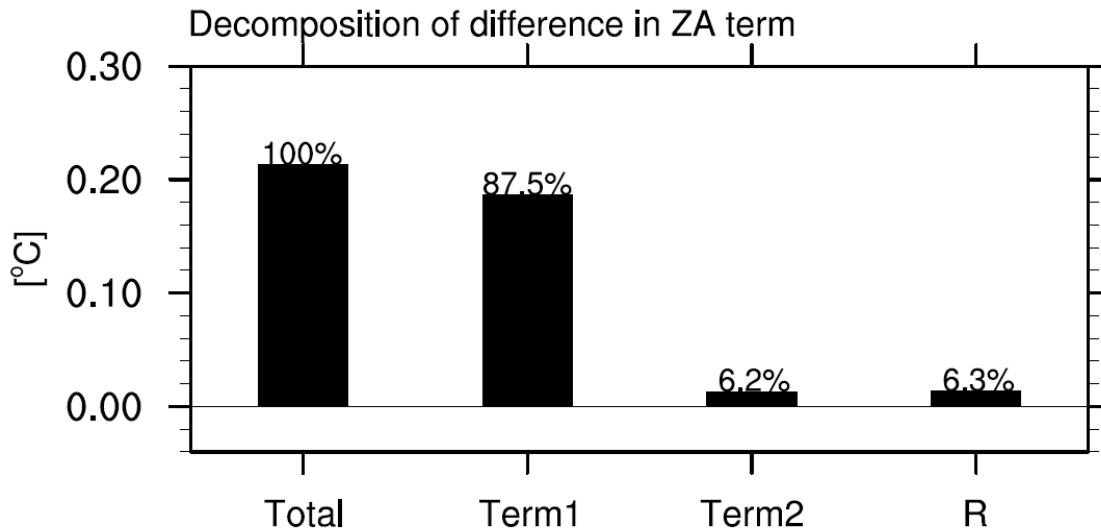
c. Anomalous zonal advection

The results from the mixed layer heat budget analysis show that the difference in the ZA term also contributes to the difference in the decay pace of the WEP SST anomalies between the two groups of models (Figs. 8, 9). Jiang et al. (2017) also argued that the bias in the WEP SST anomalies associated with ENSO in some CMIP5 models was related to the larger warm zonal advection in the WEP. In those CMIP5 models, the Pacific cold tongue extends westward excessively, leading to a larger climatological zonal SST gradient ($\frac{\partial \bar{T}}{\partial x}$) in the WEP. As a result, there is warmer zonal advection ($-u' \frac{\partial \bar{T}}{\partial x}$) under westerly wind anomalies, which could maintain the SST anomaly bias. The excessive westward extension of the Pacific cold tongue is also found in the BPMs of the CMIP6 models that show SST anomaly bias in the WEP associated with ENSO (Fig. 11c). Given that the ZA term involves both anomalous zonal current and climatological zonal SST gradient, we examine which part is the main

24

File generated with AMS Word template 2.0

contributor to the difference in the ZA term between GPMs and BPMs. The MME of the regressed ZA term of the GPMs or the BPMs can be written as $\overline{u_a * \frac{\partial T_{clm}}{\partial x}} = \overline{u_a} * \overline{\frac{\partial T_{clm}}{\partial x}} + \overline{u_a' * \left(\frac{\partial T_{clm}}{\partial x}\right)'}$, where u_a is the regressed zonal current anomalies averaged in the mixed layer. T_{clm} is the climatology of the sea water temperature averaged in the mixed layer. The overbar and prime denote the MME and the deviation from the MME, respectively. Hence, the difference in the MME of the ZA term (referred to as Total) between GPMs and BPMs (BPMs minus GPMs) can be formulated as $Total =$

$$\underbrace{(\overline{u_a}^{BPMs} - \overline{u_a}^{GPMs}) * \overline{\frac{\partial T_{clm}}{\partial x}}^{avg}}_{Term1} + \underbrace{(\overline{\frac{\partial T_{clm}}{\partial x}}^{BPMs} - \overline{\frac{\partial T_{clm}}{\partial x}}^{GPMs}) * \overline{u_a}^{avg}}_{Term2} + R,$$ where the

superscripts *BPMs*, *GPMs*, and *avg* denote the MME of the BPMs, GPMs, and their average, respectively. $Res = \overline{u_a' * \left(\frac{\partial T_{clm}}{\partial x}\right)'}^{BPMs} - \overline{u_a' * \left(\frac{\partial T_{clm}}{\partial x}\right)'}^{GPMs}$ is a residual term. Term1 and Term2 involve the contributions of the differences in anomalous zonal current and climatological zonal SST gradient, respectively. As shown in Fig. 12, the difference in the February–June accumulated ZA term is dominated by Term 1, which makes an 87.5 % contribution to the total differences, while Term 2 only accounts for 6.2 %. These results indicate that the difference in ZA term between the two groups of models is determined by the difference in anomalous zonal current.

Fig. 12. Decomposition of difference in time-accumulated zonal advection term from February(1) to June(1) during El Niño decaying year between BPMs and GPMs (BPMs minus GPMs). Total denotes the difference in zonal advection term. Term1 is the anomalous advection of mean zonal SST gradient by anomalous zonal current and Term2 is the anomalous advection of zonal SST gradient difference by mean zonal current. R is the residual term.

25

File generated with AMS Word template 2.0

To investigate the possible processes responsible for the difference in anomalous zonal current between GPMs and BPMs, the spatial patterns of regressed zonal current anomalies against the D(0)JF(1) Niño-3.4 index are shown in Fig. 13. During the El Niño mature winter, eastward current anomalies prevail in the entire equatorial Pacific in both the GPMs and the BPMs (Figs. 13a, d). The El Niño-related westerly wind stress anomalies could drive the eastward zonal current anomalies directly in the western-central equatorial Pacific (Figs. 14a, d). In addition, the westerly wind stress anomalies could produce oceanic downwelling Kelvin waves to deepen the thermocline depth in the central-eastern equatorial Pacific (Figs. 15a, d). The equatorial zonal geostrophic current is constrained by the meridional gradient of thermocline depth according to the geostrophic balance (Jin and An 1999; Chen et al. 2016a; Hu et al. 2017). The magnitude of zonal geostrophic current is thus proportional to the relative magnitude of the sea level height (SSH) in the equator with respect to the off-equatorial ones. The positive SSH anomaly in the eastern Pacific with a maximum value in the equator could lead to eastward geostrophic current anomalies *in situ* in spite of the absence of westerly wind stress (Figs. 14a, d). Note that the eastward zonal current anomalies in the western-central Pacific during El Niño mature winter are weaker in the BPMs than in the GPMs (Figs. 13a, d, g), which is probably caused by the weaker westerly wind stress anomalies (Figs. 14a, d, g) and resultant weaker equatorial SSH anomalies (Figs. 15a, d, g). Thus, a warmer zonal advection can be found in the GPMs during El Niño mature phase (Figs. 9a, c). The weaker westerly surface wind anomalies in the BPMs compared to the GPMs may be explained by the smaller increase in precipitation due to the lower sensitivity of convection to SST anomaly (Figs. 7a–c and Fig. 10d). The weaker increased precipitation and its induced diabatic heating could induce weaker westerly wind anomalies as atmospheric Rossby wave responses.

On the other hand, the westerly wind stress anomalies in the GPMs, centered at the equator with a meridional shear, correspond to positive wind stress curl anomalies off the equator, driving poleward Sverdrup transports (discharge processes) along the western-central equatorial Pacific. Consequently, a reversal of the meridional gradient of SSHA occurs in the WEP during the following spring, that is, the SSH anomalies decrease on the equator but increase off the equator (Fig. 15b). The equatorial zonal surface current anomalies thus reverse to a westward direction (Fig. 13b), against the direction of wind stress anomalies *in situ* (Fig. 14b). Besides, the equatorial SSH anomalies propagate eastward along the equator and reach the oceanic eastern boundary in El Niño mature winter as

26

File generated with AMS Word template 2.0

downwelling Kelvin waves, which are reflected as oceanic Rossby waves and propagate westward off the equators on the both hemispheres toward the central Pacific in the subsequent spring (Fig. 14b). The increased SSHs in the off-equatorial central-eastern Pacific also favor the reversal of zonal current anomalies in these regions (Fig. 13b). Therefore, the eastward zonal current anomalies reverse throughout the entire equatorial Pacific. The ZA term becomes negative and tends to dampen the warm SST anomalies over the WEP associated with ENSO. The important role of the reversed anomalous zonal current during the ENSO decaying year in the termination and transition of ENSO has been highlighted by previous studies (Jin and An 1999; Chen et al. 2016a).

However, for the BPMs, the eastward zonal current anomalies in the WEP do not reverse to westward current during the boreal spring (Fig. 13e), probably because there is no significant reversal of the meridional gradient of SSH anomalies in the WEP (Fig. 15e). The SSH anomalies on the equator of the western Pacific exhibit an insignificant change from El Niño mature winter to decaying spring (Fig. 15e). As a result, the SSH anomalies in the off-equator (5°N) are still higher than those on the equator. Such an insignificant change in SSH anomalies from ENSO mature winter to decaying spring in the BPMs (Fig. 15h) may be related to the weak westerly wind stress anomalies over the WEP during the El Niño mature winter (Figs. 14d, g), which could only induce quite weak discharge processes in this region. Because the eastward current anomalies reverse in the GPMs but not in the BPMs, the difference in zonal current anomalies in the WEP between the two groups of models is most prominent during the ENSO decaying spring, corresponding to the large difference in the ZA term between these two groups of models (Fig. 9c).

During the El Niño decaying summer, the eastward zonal current anomalies in the WEP become stronger in the BPMs (Figs. 13f, i), which is related to the persistent westerly wind stress anomalies (Figs. 14f, i). The warm SST anomalies in the WEP could weaken the Kelvin wave excited by TIO warming and induce westerly wind anomalies to its west as Rossby wave responses during boreal summer, obstructing the formation of anomalous anticyclonic circulation over the WNP (Fig. 6). Consequently, the westerly wind stress differences can be found over both the WEP and WNP regions (Figs. 14 c, f, i). The persistent westerly wind anomalies, in turn, could favor the maintenance of the SST anomalies by driving the eastward zonal current anomalies in the WEP. The positive

File generated with AMS Word template 2.0

differences in the ZA term between the BPMs and the GPMs thus still exist in the El Niño decaying summer (Fig. 9c).
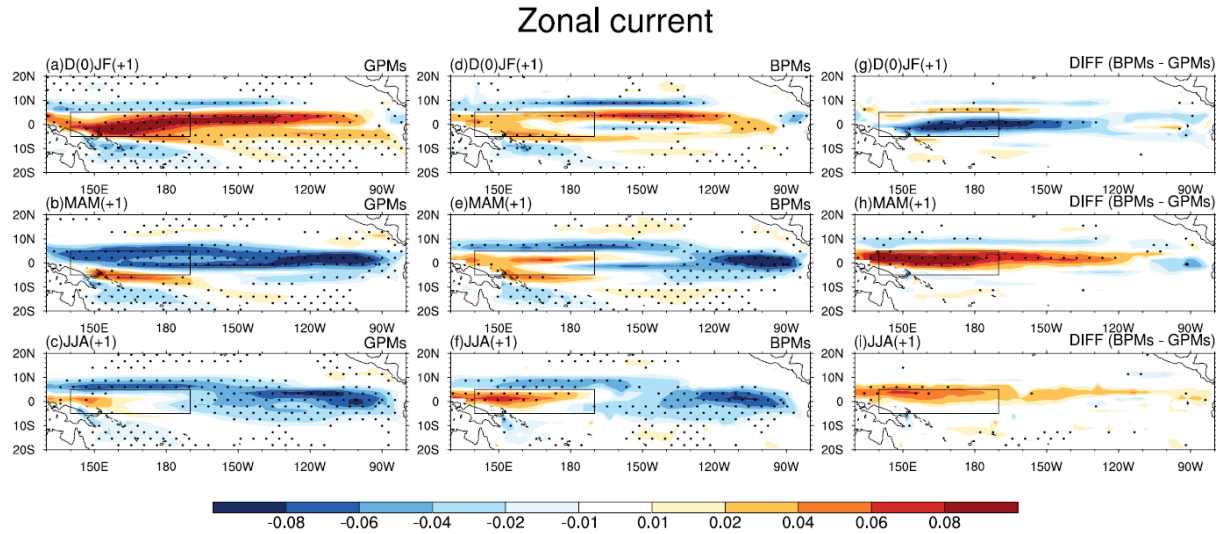
Zonal current


Fig. 13. Regressions of zonal current anomalies in the mixed layer (shading; units: m s^{-1}) during (a) ENSO mature winter (D(0)JF(1)), (b) decaying spring (MAM(1)), and (c) decaying summer (JJA(1)) onto the D(0)JF(1) Niño-3.4 index for GPMs. (d)–(f) Same as (a)–(b), but for BPMs. (g)–(i) Differences between BPMs and GPMs. Black stippling indicates that the regressed anomalies are significantly above the 95% confidence level. The black boxes indicate the western equatorial Pacific (5°S–5°N, 140°E–170°W).
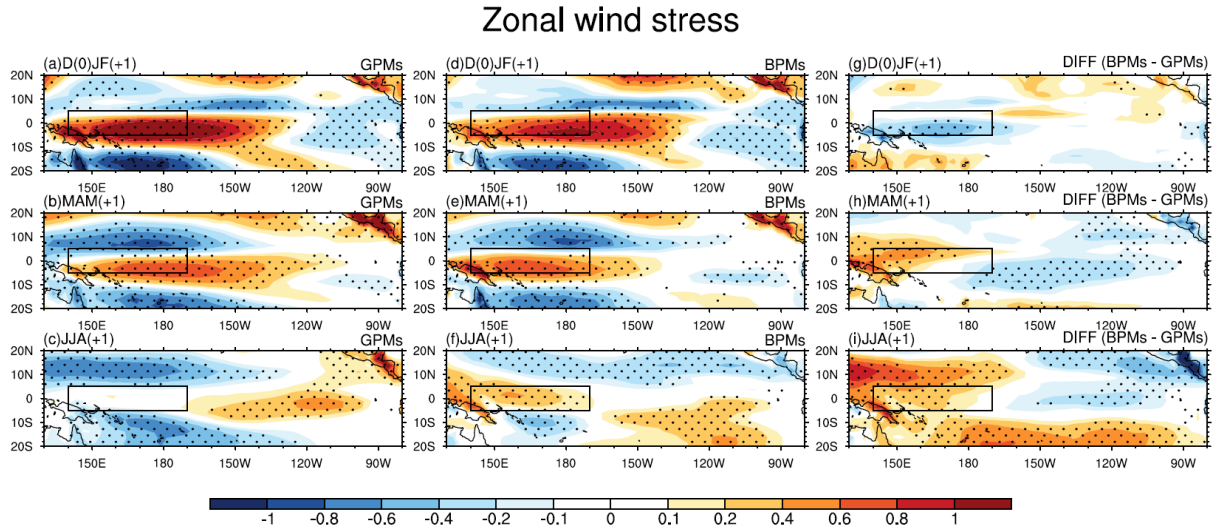
Zonal wind stress

Fig. 14. Same as in Fig. 13, but for zonal wind stress (units: 10^{-2} N m^{-2}).

28

File generated with AMS Word template 2.0

SSH
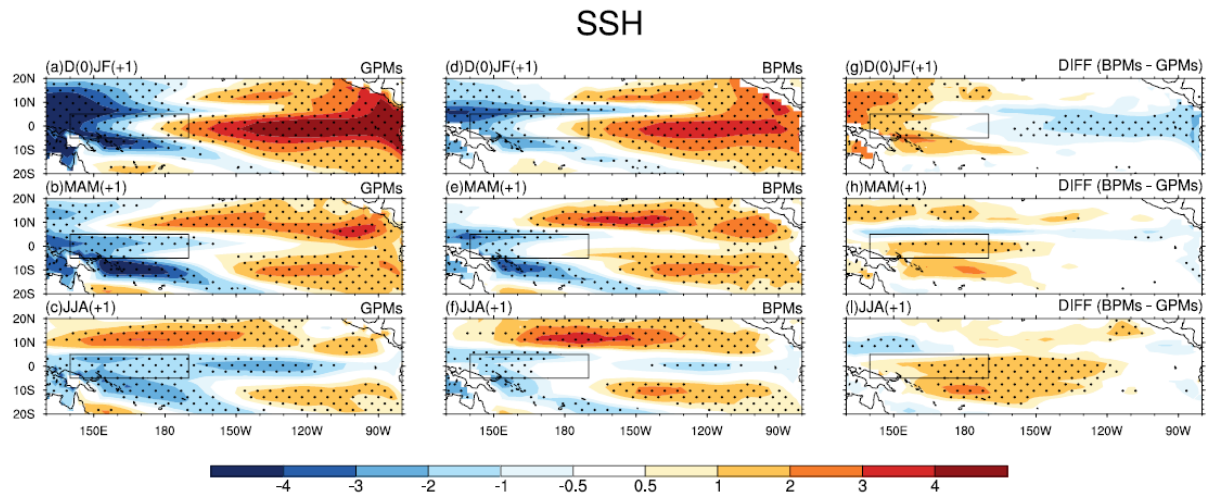
Fig. 15. Same as in Fig. 13, but for sea surface height (units: cm).

6. Conclusions and discussion

In this study, we have examined the performances of 47 CMIP6 models in simulating the impacts of ENSO on the SEASM during the ENSO decaying summer. It is found that there is larger diversity in the responses of the monsoon to ENSO among the models. Some models represent the observed SEASM anomalies during the El Niño decaying summer fairly well, including the decreased precipitation and associated anomalous anticyclonic circulation over the WNP. However, some models simulate opposite signs of the SEASM anomalies compared to observations. The main reasons for the diverse impacts are investigated by comparing the results among observations, good-performance models, and bad-performance models, which are summarized in Fig. 16.

The inter-model differences in the ENSO-related SEASM anomalies are highly associated with the simulated SST anomalies in the WEP during the ENSO decaying summer. Those models that perform well in representing the ENSO-related SEASM anomalies display low WEP SST anomalies that are close to the observed values over the WEP. However, for those models with less skill in simulating the SEASM responses to El Niño, the warm SST anomalies persist in the El Niño decaying summer rather than dissipating as in observations. The unabated warm SST anomalies could weaken the warm Kelvin wave emanating from the TIO by reducing the zonal gradient of SST anomaly between TIO and WEP. On the other hand, they can generate an increase in precipitation and result in westerly wind anomalies over the WNP. Consequently, the formation of anomalous anticyclonic circulation and the associated decreased SEASM precipitation during El Niño decaying summer cannot be found in these models. The deficiency of these models in capturing the observed ENSO-related

29

SEASM anomalies, therefore, could be mainly attributed to the bias of the WEP SST anomalies during the ENSO decaying summer.

A quantitative mixed-layer heat budget analysis suggests that the slow decay of WEP SST anomalies in the BPMs is primarily caused by the weak SW radiation feedback. Although the WEP SST warming in the BPMs is comparable to that in the GPMs during El Niño mature winter and decaying spring, the positive precipitation anomaly in the WEP is significantly smaller in the BPMs than in the GPMs due to the lower sensitivity of precipitation to local SST anomaly, which leads to a weak reflection of SW radiation. The bias in the precipitation sensitivity to local SST anomaly could be attributed to the cold bias of the climatological SST over the WEP in the BPMs, which is associated with the excessive shrinkage of the western Pacific warm pool and the excessive westward extension of the Pacific cold tongue. On the other hand, in the BPMs the anomalous warm zonal advection in the WEP can persist from the El Niño mature phase to decaying summer, which also contributes to the slow decay of WEP SST anomalies. This is because the El Niño-related anomalous eastward current in the WEP does not reverse to the westward current from the El Niño mature winter to decaying spring as in the GPMs since the reversal of the meridional gradient of SSH anomaly does not occur in the WEP. Such differences in the time evolutions of SSH anomalies in the WEP between BPMs and GPMs may be attributed to the weak discharge processes from the El Niño mature winter to decaying spring for the BPMs. The weakly enhanced precipitation over the WEP in the BPMs during the El Niño mature phase results in smaller westerly wind anomalies and thus weaker poleward Sverdrup transports in the WEP.

This study suggests that the models need to improve their skills in simulating the evolution of SST anomaly in the WEP during the ENSO decaying phase to better capture the delayed impacts of ENSO on the SEASM. In addition, our results indicate that the bias in the WEP SST anomaly associated with ENSO could be attributed to the unrealistic atmospheric feedback induced by the climatological SST bias. Furthermore, it has been suggested that in the western Pacific, convection is most sensitive to the change in SST during the boreal winter and spring since the climatological SST is close to the SST threshold in these seasons (Lin et al. 2022). To produce a more realistic air-sea interaction in the western Pacific, climate models thus also need to improve their performance in representing the climatological SST.

File generated with AMS Word template 2.0

Previous studies have highlighted the important role of ENSO decaying pace in modulating the intensity of WNPAC during ENSO decaying summer (Chen et al. 2012, 2016a; Jiang et al. 2019; Wu et al. 2020). The ENSO events with short decaying (long persistent) phase could lead to a strong (weak) WNPAC. Nevertheless, the difference in ENSO decaying pace between BPMs and GPMs is insignificant (Fig. S5). Although in the BPMs the discharge processes are weak over the WEP, they could be comparable to those in the GPMs over the central-eastern Pacific due to the comparable surface westerly wind stress anomalies over this region (Fig. 14g). We also conducted the mixed-layer heat budget analysis for the Niño-3.4 region. It was found that the difference in net heat flux (Q) could be offset by the difference in meridional advection associated with meridional current anomaly (VA; $-v'\frac{\partial \bar{T}}{\partial y}$), leading to an approximately equal decaying rate of ENSO between the GPMs and the BPMs (figure not shown). The reasons for the distinct differences in VA term are beyond the scope of this study and need to be further explored. On the other hand, the regression method used in this paper does not discern the effect of concurrent ENSO SST anomalies, but there may be another ENSO event developing in the summer. To assess the influences of the diversity in ENSO evolution in the diverse ENSO-SEASM relationship among CMIP6 models, we divide the El Niño (La Niña) events into two types 1-yr and 2-yr El Niño (La Niña) by following Wu et al. (2019), referred to as decaying and persistent El Niño (La Niña), respectively (Fig. S9). Although the two types of ENSO exert different impacts on the SEASM (Fig. S10), the Niño-3.4 SST anomalies during the JJA(1) in these two types of ENSO events do not exhibit significant differences between GPMs and the BPMs (Fig. S9). However, the BPMs cannot simulate the summertime WNP anticyclone (cyclone) in both decaying and persistent El Niño (La Niña), and the most prominent differences in SST anomalies during JJA(1) between the two groups of models are still in the WEP (Fig. S10), with significantly warmer (colder) values in BPMs than in GPMs associated with El Niño (La Niña) (Fig. S11). These composite results reconfirm that the main cause of the diverse ENSO-SEASM relationship is the bias in the WEP SST anomaly, and the influence of concurrent ENSO SST anomaly on the diverse relationship could be weak. One interesting result is that there is a relatively weaker biennial tendency of ENSO in BPMs than that in GPMs since the ratio of persistent El Niño in the BPMs (38%) is higher than that in the GPMs (26%) by about 12% (Fig. S9). It has been suggested that the El Niño-induced WNPAC during the decaying summer may favor the transition of El Niño into La Niña by inducing oceanic downwelling Kelvin waves propagating eastward along the equatorial

31

File generated with AMS Word template 2.0

Pacific, thereby enhancing the biennial tendency of ENSO (Wang et al. 1999; Wang et al. 2001; Li et al. 2007). Therefore, one possible reason why the ENSO biennial oscillation is weak in the BPMs could be that these models cannot simulate the correct response of SEASM to ENSO, resulting in weak monsoon's feedbacks on ENSO.

In addition to the diverse ENSO evolutions, the considerable diversity in the SST anomaly pattern of ENSO has also been well known. The central Pacific El Niño, characterized by maximum SST anomalies in the central ocean, has occurred more frequently in the recent decades (Ashok et al. 2007; Kao and Yu 2009). Moreover, it has been reported that the central Pacific El Niño also exerts a delayed effect on the EASM (Feng et al. 2011, 2019). Although the current study has investigated the skill of CMIP6 models in simulating the impact of ENSO on the SEASM, further investigations are needed to understand the model performance in depicting the impacts of different types of ENSO on the monsoon.
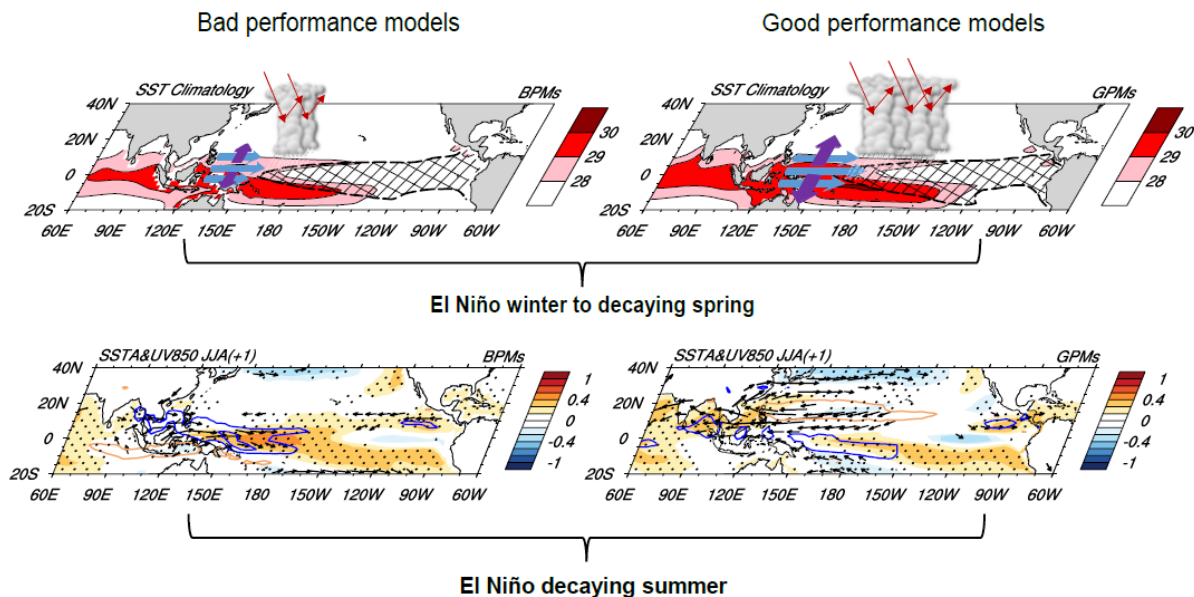
Fig. 16. Schematic diagram illustrating the physical processes responsible for the difference in SEASM response to El Niño between BPMs and GPMs. In the upper panels, the black hatching denotes the warm SST anomalies of El Niño. The shading denotes climatological SST. The red arrows denote the reflected SW radiation. The blue arrows denote the westerly wind anomalies caused by El Niño SST warming. The purple arrows indicate the poleward Sverdrup transport due to positive wind stress curl anomalies. The regressed JJA(1) SST (shading), precipitation (contours) and 850-hPa wind anomalies (vectors) upon the D(0)JF(1) Niño-3.4 index are shown in the bottom panels.

32

File generated with AMS Word template 2.0

Data Availability Statement.

The HadISST dataset was downloaded from the UK Met Office at https://www.metoffice.gov.uk. The GPCP monthly precipitation data is provided by the NOAA PSL, Boulder, Colorado, USA, from the website at https://psl.noaa.gov/data/gridded/data.gpcp.html. The ERA5 monthly reanalysis data can be downloaded from https://cds.climate.copernicus.eu/cdsapp#!/dataset/reanalysis-era5-pressure-levels-monthly-means?tab=form. NCEP-NCAR data is from https://psl.noaa.gov/data/gridded/data.ncep.reanalysis.html. The CMIP6 model datasets are available at the Earth System Grid Federation (ESGF; at http://esgf-node.llnl.gov/search/cmip6).

REFERENCES

Adler, R. F., and Coauthors, 2003: The version-2 global precipitation climatology project (GPCP) monthly precipitation analysis (1979–Present). *J. Hydrometeorol.*, **4**, 1147–1167, https://doi.org/10.1175/1525-7541(2003)004<1147:TVGPCP>2.0.CO;2.

An, S. I., and B. Wang, 2001: Mechanisms of locking of the El Niño and La Niña mature phases to boreal winter. *J. Climate*, **14**, 2164–2176, https://doi.org/10.1175/1520-0442(2001)014<2164:MOLOTE>2.0.CO;2.

Ashok, K., S. K. Behera, S. A. Rao, H. Weng, and T. Yamagata, 2007: El Niño Modoki and its possible teleconnection. *J. Geophys. Res. Ocean.*, **112**, 1–27, https://doi.org/10.1029/2006JC003798.

Cao, J., R. Lu, J. Hu, and H. Wang, 2013: Spring Indian Ocean-western Pacific SST contrast and the East Asian summer rainfall anomaly. *Adv. Atmos. Sci.*, **30**, 1560–1568, https://doi.org/10.1007/S00376-013-2298-6/METRICS.

Chang, C. P., Y. Zhang, and T. Li, 2000: Interannual and interdecadal variations of the East Asian summer monsoon and tropical pacific SSTs. Part I: Roles of the subtropical ridge.

File generated with AMS Word template 2.0

Accepted for publication in *Journal of Climate*. DOI 10.1175/JCLI-D-23-0303.1.

      J. Climate, **13**, 4326–4340, https://doi.org/10.1175/1520-
      0442(2000)013<4326:IAIVOT>2.0.CO;2.

Chen, H.-C., Z.-Z. Hu, B. Huang, and C.-H. Sui, 2016a: The role of reversed equatorial zonal
      transport in terminating an ENSO event. J. Climate, 29, 5859–5877,
      https://doi.org/10.1175/JCLI-D-16-0047.1.

Chen, W., J.-K. Park, B. Dong, R. Lu, and W.-S. Jung, 2012: The relationship between El
      Niño and the western North Pacific summer climate in a coupled GCM: Role of the
      transition of El Niño decaying phases. *J. Geophys. Res.*, **117**, D12
      111, https://doi.org/10.1029/2011JD017385.

Chen, W., J.-Y. Lee, K.-J. Ha, K.-S. Yun, and R. Lu, 2016b: Intensification of the western
      North Pacific anticyclone response to the short decaying El Niño event due to
      greenhouse warming. *J. Climate*, **29**, 3607–3627, https://doi.org/10.1175/JCLI-D-15-
      0195.1.

Chou, C., L. F. Huang, J. Y. Tu, L. Tseng, and Y. C. Hsueh, 2009: El Niño impacts on
      precipitation in the western North Pacific–East Asian sector. *J. Climate*, **22**, 2039–2057,
      https://doi.org/10.1175/2008JCLI2649.1.

Chowdary, J. S., A. Parekh, and C. Gnanaseelan, 2021: *Indian Summer Monsoon Variability:*
      El Niño–Teleconnections and Beyond. 1st ed. Elsevier, 472 pp.

Collins, M., and Coauthors, 2010: The impact of global warming on the tropical Pacific
      Ocean and El Niño. *Nat. Geosci.*, **3**, 391–397, https://doi.org/10.1038/ngeo868.

Eyring, V., S. Bony, G. A. Meehl, C. A. Senior, B. Stevens, R. J. Stouffer, and K. E. Taylor,
      2016: Overview of the Coupled Model Intercomparison Project Phase 6 (CMIP6)
      experimental design and organization. *Geosci. Model Dev.*, **9**, 1937–1958,
      https://doi.org/10.5194/GMD-9-1937-2016.

——, and Coauthors, 2019: Taking climate model evaluation to the next level. *Nat. Climate*
      Chang, **9**, 102–110, https://doi.org/10.1038/s41558-018-0355-y.

Feng, J., W. Chen, C. Y. Tam, and W. Zhou, 2011: Different impacts of El Niño and El Niño
      Modoki on China rainfall in the decaying phases. *Int. J. Climatol.*, **31**, 2091–2101,
      https://doi.org/10.1002/JOC.2217.

File generated with AMS Word template 2.0

——, ——, H. Gong, J. Ying, and W. Jiang, 2019: An investigation of CMIP5 model biases in simulating the impacts of central Pacific El Niño on the East Asian summer monsoon. *Climate Dyn.*, **52**, 2631–2646, https://doi.org/10.1007/S00382-018-4284-2/FIGURES/13.

Gadgil, S., P. V. Joseph, and N. V. Joshi, 1984: Ocean-atmosphere coupling over monsoon regions. *Nature*, **312**, 141–143, https://doi.org/10.1038/312141a0.

Gill, A. E., 1980: Some simple solutions for heat- induced tropical circulation. *Quart. J. Roy. Meteorol. Soc.*, **106**, 447–462, https://doi.org/10.1002/qj.49710644905.

Graham, N. E., and T. P. Barnett, 1987: Sea surface temperature, surface wind divergence, and convection over tropical oceans. *Science*, **238**, 657–659, https://doi.org/10.1126/science.238.4827.657.

Griffies, S. M., and Coauthors, 2016: OMIP contribution to CMIP6: Experimental and diagnostic protocol for the physical component of the Ocean Model Intercomparison Project. *Geosci. Model Dev.*, **9**, 3231–3296, https://doi.org/10.5194/gmd-9-3231-2016.

Hayes, S. P., Ping Chang, and M. J. McPhaden, 1991: Variability of the sea surface temperature in the eastern equatorial Pacific during 1986–1988. *J. Geophys. Res. Ocean.*, **96**, 10553–10566, https://doi.org/10.1029/91JC00942.

He, C., and T. Zhou, 2015: Responses of the western North Pacific subtropical high to global warming under RCP4.5 and RCP8.5 scenarios projected by 33 CMIP5 models: The dominance of tropical Indian Ocean–tropical western Pacific SST gradient. *J. Climate*, **28**, 365–380, https://doi.org/10.1175/JCLI-D-13-00494.1.

He, C., Z. Cui, and C. Wang, 2022: Response of western North Pacific anomalous anticyclones in the summer of decaying El Niño to global warming: Diverse projections based on CMIP6 and CMIP5 models. *J. Climate*, **35**, 359–372, https://doi.org/10.1175/JCLI-D-21-0352.1.

He, J., N. C. Johnson, G. A. Vecchi, B. Kirtman, A. T. Wittenberg, and S. Sturm, 2018: Precipitation sensitivity to local variations in tropical sea surface temperature. *J. Climate*, **31**, 9225–9238, https://doi.org/10.1175/JCLI-D-18-0262.1.

Hersbach, H., and Coauthors, 2020: The ERA5 global reanalysis. *Quart. J. Roy. Meteorol. Soc.*, **146**, 1999–2049, https://doi.org/10.1002/QJ.3803.

35

File generated with AMS Word template 2.0

Hu, K., G. Huang, X.-T. Zheng, S.-P. Xie, X. Qu, Y. Du, and L. Liu, 2014: Interdecadal variations in ENSO influences on Northwest Pacific–East Asian early summertime climate simulated in CMIP5 models. *J. Climate*, **27**, 5982–5998, https://doi.org/10.1175/JCLI-D-13-00268.1.

Hu, Z.-Z., A. Kumar, B. Huang, J. Zhu, R.-H. Zhang, and F.-F. Jin, 2017: Asymmetric evolution of El Niño and La Niña : the recharge / discharge processes and role of the off-equatorial sea surface height anomaly. *Climate Dyn.*, **49**, 2737–2748, https://doi.org/10.1007/s00382-016-3498-4.

Huang, R., and Y. Wu, 1989: The influence of ENSO on the summer climate change in China and its mechanism. *Adv. Atmos. Sci.*, **6**, 21–32, https://doi.org/10.1007/BF02656915.

——, and F. Sun, 1992: Impacts of the tropical western Pacific on the East Asian summer monsoon. *J. Meteorol. Soc. Japan*, **70**, 243–256.

Jiang, D., D. Hu, Z. Tian, and X. Lang, 2020: Differences between CMIP6 and CMIP5 models in simulating climate over China and the East Asian monsoon. *Adv. Atmos. Sci.*, **37**, 1102–1118, https://doi.org/10.1007/S00376-020-2034-Y/METRICS.

Jiang, W., G. Huang, K. Hu, R. Wu, H. Gong, X. Chen, and W. Tao, 2017: Diverse relationship between ENSO and the northwest Pacific summer climate among CMIP5 models: Dependence on the ENSO decay pace. *J. Climate*, **30**, 109–127, https://doi.org/10.1175/JCLI-D-16-0365.1.

——, ——, P. Huang, and K. Hu, 2018: Weakening of northwest Pacific anticyclone anomalies during post–El Niño summers under global warming. *J. Climate*, 31, 3539–3555, https://doi.org/10.1175/JCLI-D-17-0613.1.

——, ——, P. Huang, R. Wu, K. Hu, and W. Chen, 2019: Northwest Pacific anticyclonic anomalies during post–El Niño summers determined by the pace of El Niño decay. *J. Climate*, **32**, 3487–3503, https://doi.org/10.1175/JCLI-D-18-0793.1.

——, P. Huang, G. Huang, and J. Ying, 2021: Origins of the excessive westward extension of ENSO SST simulated in CMIP5 and CMIP6 models. *J. Climate*, **34**, 2839–2851, https://doi.org/10.1175/JCLI-D-20-0551.1.

Jin, F., and S. An, 1999: Thermocline and zonal advective feedbacks within the equatorial ocean recharge oscillator model for ENSO. *Geophys. Res. Lett.*, **26**, 2989–2992.

File generated with AMS Word template 2.0

Johnson, N. C., and S. P. Xie, 2010: Changes in the sea surface temperature threshold for tropical convection. *Nat. Geosci.*, **3**, 842–845, https://doi.org/10.1038/ngeo1008.

Kalnay, E., W. Collins, D. Deaven, L. Gandin, M. Iredell, R. Jenne, and D. Joseph, 1996: The NCEP/NCAR 40-year reanalysis project. *Bull. Amer. Meteorol. Soc.*, **77**, 437–472.

Kao, H.-Y., and J.-Y. Yu, 2009: Contrasting eastern-Pacific and central-Pacific types of El Ni Niño. *J. Climate*, **22**, 615–632, https://doi.org/https://doi.org/10.1175/2008JCLI2309.1.

Kim, S. T., and J. Y. Yu, 2012: The two types of ENSO in CMIP5 models. *Geophys. Res. Lett.*, **39**, 11704, https://doi.org/10.1029/2012GL052006.

Kug, J. S., Y. G. Ham, J. Y. Lee, and F. F. Jin, 2012: Improved simulation of two types of El Niño in CMIP5 models. *Environ. Res. Lett.*, **7**, 034002, https://doi.org/10.1088/1748-9326/7/3/034002.

Lau, K.-M., K.-M. Kim, and S. Yang, 2000: Dynamical and boundary forcing characteristics of regional components of the Asian summer monsoon. *J. Climate*, **13**, 2461–2482, https://doi.org/10.1175/1520-0442(2000)013.

Lau, K. M., H. T. Wu, and S. Bony, 1997: The role of large-scale atmospheric circulation in the relationship between tropical convection and sea surface temperature. *J. Climate*, **10**, 381–392, https://doi.org/10.1175/1520-0442(1997)010<0381:TROLSA>2.0.CO;2.

Lee, S. S., J. Y. Lee, K. J. Ha, B. Wang, and J. K. E. Schemm, 2011: Deficiencies and possibilities for long-lead coupled climate prediction of the western North Pacific-East Asian summer monsoon. *Climate Dyn.*, **36**, 1173–1188, https://doi.org/10.1007/S00382-010-0832-0/FIGURES/13.

Li, S., J. Lu, G. Huang, and K. Hu, 2008: Tropical Indian Ocean basin warming and East Asian summer monsoon: A multiple AGCM study. *J. Climate*, **21**, 6080–6088, https://doi.org/10.1175/2008JCLI2433.1.

Li, T., and B. Wang, 2005: A review on the western North Pacific monsoon: Synoptic-to-interannual variabilities. *Terr. Atmos. Ocean. Sci.*, **16**, 285–314, https://doi.org/10.3319/TAO.2005.16.2.285(A).

Li, Y., R. Y. Lu, and B. W. Dong, 2007: The ENSO–Asian monsoon interaction in a coupled ocean–atmosphere GCM. *J. Climate*, **20 ,** 5164–5177.

Li, Z., and S. Yang, 2017: Influences of spring-to-summer sea surface temperatures over different Indian Ocean domains on the Asian summer monsoon. *Asia-Pacific J. Atmos. Sci.*, **53**, 471–487, https://doi.org/10.1007/S13143-017-0050-3/METRICS.

——, ——, B. He, and C. Hu, 2016: Intensified springtime deep convection over the South China Sea and the Philippine Sea dries southern China. *Sci. Rep.*, **6**, 1–9, https://doi.org/10.1038/srep30470.

Liao, H., C. Wang, and Z. Song, 2021: ENSO phase-locking biases from the CMIP5 to CMIP6 models and a possible explanation. *Deep. Res. Part II Top. Stud. Oceanogr.*, **189–190**, 104943, https://doi.org/10.1016/j.dsr2.2021.104943.

Lin, S., S. Yang, S. He, Z. Li, J. Chen, W. Dong, and J. Wu, 2022: Attribution of the seasonality of atmospheric heating changes over the western tropical Pacific with a focus on the spring season. *Climate Dyn.*, **58**, 2575–2592, https://doi.org/10.1007/s00382-021-06020-3.

Lindzen, R. S., and S. Nigam, 1987: On the role of sea surface temperature gradients in forcing low-level winds and convergence in the tropics. *J. Atmos. Sci.*, **44**, 2418–2436, https://doi.org/10.1175/1520-0469(1987)044<2418:otross>2.0.co;2.

Lu, M., S. Yang, J. Wang, Y. Wu, and X. Jia, 2021: Response of regional Asian summer monsoons to the effect of reduced surface albedo in different Tibetan Plateau domains in idealized model experiments. *J. Climate,* **34,** 7023–7036.

Lu, M., S. Yang, C. Zhu, J. Wang, S. Lin, W. Wei, and H. Fan, 2023: Thermal impact of the southern Tibetan Plateau on the southeast Asian summer monsoon and modulation by the tropical Atlantic SST. *J. Climate*, **36**, 1319–1330, https://doi.org/10.1175/JCLI-D-22-0493.1.

Lu, R., and B. Dong, 2005: Impact of Atlantic sea surface temperature anomalies on the summer climate in the western North Pacific during 1997–1998. *J. Geophys. Res. Atmos.*, **110**, 1–11, https://doi.org/10.1029/2004JD005676.

Meehl, G. A., C. Covey, T. Delworth, M. Latif, B. McAvaney, J. F. B. Mitchell, R. J. Stouffer, and K. E. Taylor, 2007: The WCRP CMIP3 multimodel dataset: A new era in climate change research. *Bull. Amer. Meteorol. Soc.*, **88**, 1383–1394, https://doi.org/10.1175/BAMS-88-9-1383.

File generated with AMS Word template 2.0

Nitta, T., 1987: Convective activities in the tropical western Pacific and their impact on the Northern Hemisphere summer circulation. *J. Meteorol. Soc. Japan*, **65**, 373–390.

Qu, T., 2003: Mixed layer heat balance in the western North Pacific. *J. Geophys. Res. Ocean.*, **108**, 1–13, https://doi.org/10.1029/2002jc001536.

Rayner, N. A., D. E. Parker, E. B. Horton, C. K. Folland, L. V. Alexander, D. P. Rowell, E. C. Kent, and A. Kaplan, 2003: Global analyses of sea surface temperature, sea ice, and night marine air temperature since the late nineteenth century. *J. Geophys. Res. Atmos.*, **108**, 4407, https://doi.org/10.1029/2002jd002670.

Rong, X. Y., R. H. Zhang, and T. Li, 2010: Impacts of Atlantic sea surface temperature anomalies on Indo-East Asian summer monsoon-ENSO relationship. *Chinese Sci. Bull.*, **55**, 2458–2468, https://doi.org/10.1007/s11434-010-3098-3.

Song, F., and T. Zhou, 2014: The climatology and interannual variability of East Asian summer monsoon in CMIP5 coupled models: Does air–sea coupling improve the simulations? *J. Climate*, **27**, 8761–8777, https://doi.org/10.1175/JCLI-D-14-00396.1.

——, and ——, 2015: The crucial role of internal variability in modulating the decadal variation of the East Asian summer monsoon–ENSO relationship during the twentieth century. *J. Climate*, **28**, 7093–7107, https://doi.org/10.1175/JCLI-D-14-00783.1.

Sun, C., and Coauthors, 2022: The warming and wetting ecological environment changes over the Qinghai-Tibetan Plateau and the driving effect of the Asian summer monsoon. *J. Trop. Meteorol.,* **28**, 95–108.

Tao, W., G. Huang, K. Hu, H. Gong, G. Wen, and L. Liu, 2016: A study of biases in simulation of the Indian Ocean basin mode and its capacitor effect in CMIP3/CMIP5 models. *Climate Dyn.*, **46**, 205–226, https://doi.org/10.1007/S00382-015-2579-0/FIGURES/19.

Taylor, K. E., R. J. Stouffer, and G. A. Meehl, 2012: An overview of CMIP5 and the experiment design. *Bull. Amer. Meteorol. Soc.*, **93**, 485–498, https://doi.org/10.1175/BAMS-D-11-00094.1.

Terao, T., and T. Kubota, 2005: East-west SST contrast over the tropical oceans and the post El Niño western North Pacific summer monsoon. *Geophys. Res. Lett.*, **32**, https://doi.org/10.1029/2005GL023010.

39

File generated with AMS Word template 2.0

Tziperman, E., S. E. Zebiak, and M. A. Cane, 1997: Mechanisms of seasonal-ENSO interaction. *J. Atmos. Sci.*, **54**, 61–71, https://doi.org/10.1175/1520-0469(1997)054<0061:MOSEI>2.0.CO;2.

Uppala, S. M., and Coauthors, 2005: The ERA-40 re-analysis. *Quart. J. Roy. Meteorol. Soc.*, **131**, 2961–3012, https://doi.org/10.1256/qj.04.176.

Vecchi, G. A., and B. J. Soden, 2007: Effect of remote sea surface temperature change on tropical cyclone potential intensity. *Nature*, **450,** 1066–1070.

Waliser, D. E., and N. E. Graham, 1993: Convective cloud systems and warm-pool sea surface temperatures: Coupled interactions and self-regulation. *J. Geophys. Res. Atmos.*, **98**, https://doi.org/10.1029/93jd00872.

Wang, B., and Z. Fan, 1999: Choice of South Asian summer monsoon indices. *Bull. Amer. Meteorol. Soc.*, **80**, 629–638, https://doi.org/10.1175/1520-0477(1999)080<0629:COSASM>2.0.CO;2.

——, and LinHo, 2002: Rainy season of the Asian-Pacific summer monsoon. *J. Climate*, **15**, 386–398, https://doi.org/10.1175/1520-0442(2002)015<0386:RSOTAP>2.0.CO;2.

——, W. Renguang, and F. Xiuhua, 2000: Pacific–East Asian Teleconnection: How does ENSO affect East Asian climate? *J. Climate*, **13**, 1517–1536, https://doi.org/10.1175/1520-0442(2000)013<1517:PEATHD>2.0.CO;2.

Wang, B., R. Wu, and K. M. Lau, 2001: Interannual variability of the Asian summer monsoon: Contrasts between the Indian and the western North Pacific-East Asian monsoons. *J. Climate*, **14**, 4073–4090, https://doi.org/10.1175/1520-0442(2001)014<4073:IVOTAS>2.0.CO;2.

Wang, B., R. Wu, R. Lukas, and S. I. An, 2001: A possible mechanism for ENSO turnabout. *Dynamics of Atmospheric General Circulation and Climate*, IAP/Academia Sinica, Eds., China Meteorological Press, 552–578.

Wang, B., B. Xiang, and J. Y. Lee, 2013: Subtropical high predictability establishes a promising way for monsoon and tropical storm predictions. *Proc. Natl. Acad. Sci. U. S. A.*, **110**, 2718–2722.

File generated with AMS Word template 2.0

Wang, B., J. Yang, T. Zhou, B. Wang, 2008: Interdecadal changes in the major modes of Asian-Australian monsoon variability: Strengthening relationship with ENSO since the late 1970s. *J. Climate*, **21**, 1771–1789.

Wang, C., R. H. Weisberg, and J. I. Virmani, 1999: Western Pacific interannual variability associated with the El Niño–Southern Oscillation. *J. Geophys. Res.*, **104**, 5131–5149, https://doi.org/10.1029/1998JC900090.

Wang, L., S. Guo, and G. Jing, 2016: The timing of South-Asian high establishment and its relation to tropical Asian summer monsoon and precipitation over east-central China in summer. *J. Trop. Meteorol.,* **22**, 136–144.

Wang, W., and M. J. McPhaden, 2001: Surface layer temperature balance in the equatorial Pacific during the 1997-98 El Niño and 1998-99 La Niña. *J. Climate.*, **14**, 3393–3407, https://doi.org/10.1175/1520-0442(2001)014<3393:SLTBIT>2.0.CO;2.

Wu, B., and T. Zhou, 2016: Relationships between ENSO and the East Asian–western North Pacific monsoon: observations versus 18 CMIP5 models. *Climate Dyn.*, **46**, 729–743, https://doi.org/10.1007/S00382-015-2609-Y.

Wu, B., T. Li, and T. Zhou, 2010: Relative contributions of the Indian Ocean and local SST anomalies to the maintenance of the western North Pacific anomalous anticyclone during the El Niño decaying summer. *J. Climate*, **23**, 2974–2986, https://doi.org/10.1175/2010JCLI3300.1.

Wu, B., T. Zhou, and T. Li, 2017a: Atmospheric dynamic and thermodynamic processes driving the western North Pacific anomalous anticyclone during El Niño. Part I: Maintenance mechanisms. *J. Climate*, **30**, 9621–9635, https://doi.org/10.1175/JCLI-D-16-0489.1.

Wu, B., T. Zhou, and T. Li, 2017b: Atmospheric dynamic and thermodynamic processes driving the western North Pacific anomalous anticyclone during El Niño. Part II: Formation processes. *J. Climate*, **30**, 9637–9650, https://doi.org/10.1175/JCLI-D-16-0495.1.

Wu, M., T. Zhou, X. Chen, and B. Wu, 2020: Intermodel uncertainty in the projection of the anomalous western North Pacific anticyclone associated with El Niño under global warming. *Geophys. Res. Lett.*, **47**, https://doi.org/10.1029/2019GL086139.

File generated with AMS Word template 2.0

——, ——, and ——, 2021: The source of uncertainty in projecting the anomalous western North Pacific anticyclone during El Niño–decaying summers. *J. Climate*, **34**, 6603–6617, https://doi.org/10.1175/JCLI-D-20-0904.1.

Wu, X., Y. M. Okumura, and P. N. DiNezio, 2019: What controls the duration of El Niño and La Niña events? *J. Climate*, **32**, 5941–5965, https://doi.org/10.1175/JCLI-D-18-0681.1.

Xiang, B., B. Wang, W. Yu, and S. Xu, 2013: How can anomalous western North Pacific subtropical high intensify in late summer? *Geophys. Res. Lett.*, **40**, 2349–2354, https://doi.org/10.1002/GRL.50431.

Xie, S. P., K. Hu, J. Hafner, H. Tokinaga, Y. Du, G. Huang, and T. Sampe, 2009: Indian Ocean capacitor effect on Indo-Western Pacific climate during the summer following El Niño. *J. Climate*, **22**, 730–747, https://doi.org/10.1175/2008JCLI2544.1.

Xin, X., T. Wu, J. Zhang, J. Yao, and Y. Fang, 2020: Comparison of CMIP6 and CMIP5 simulations of precipitation in China and the East Asian summer monsoon. *Int. J. Climatol.*, **40**, 6423–6440, https://doi.org/10.1002/JOC.6590.

Yang, J., Q. Liu, S. P. Xie, Z. Liu, and L. Wu, 2007: Impact of the Indian Ocean SST basin mode on the Asian summer monsoon. *Geophys. Res. Lett.*, **34**, 1–5, https://doi.org/10.1029/2006GL028571.

Yoo, S.-H., S. Yang, and C.-H. Ho, 2006: Variability of the Indian Ocean sea surface temperature and its impacts on Asian-Australian monsoon climate. *J. Geophys. Res.,* **111,** D03108, doi:10.1029/2005JD006001.

Zhang, C., 1993: Large-scale variability of atmospheric deep convection in relation to sea surface temperature in the tropics. *J. Climate*, **6**, 1898–1913.

File generated with AMS Word template 2.0